International Tables for Crystallography (2018). Vol. H, Chapter 1.1, pp. 2–23.

1.1. Overview and principles of powder diffraction

R. E. Dinnebier and S. J. L. Billinge

1.1.1. Information content of a powder pattern

The structures of real materials comprise not only the crystal structure – the time- and space-averaged periodic configuration of atoms on an idealized periodic lattice – but also the microstructure, which is caused by imperfections, dislocations and all kinds of disorder. The microstructure is often responsible for interesting properties of the material. A powder diffraction pattern contains a wealth of information about this microstructure in addition to the average crystal structure, as shown schematically in Fig. 1.1.1.

At each stage of a powder diffraction study, great effort and ingenuity are needed to find the optimal experimental conditions and to understand and analyse the resulting line shapes and signals. As experimental equipment, theoretical understanding and computational tools have improved, it has become possible to tap into the rich information content of the line peak shapes and diffuse background of a typical powder diffraction pattern, yielding unprecedented information about real materials for materials scientists, chemists, physicists, earth scientists and engineers. For example, in the modern practice of whole-pattern modelling, the line profile is calculated from first principles, taking into account all aspects of the state of the sample, such as particle-size distributions, inhomogeneous strains and texture, as well as the experimental setup and aberrations. There is a useful feedback effect in that better profile descriptions result in more accurate determinations of the intensities of the Bragg peaks, which is important to extract accurate structural information (Bragg peaks are introduced in detail in the next section). Similarly, great progress has been made in the extraction of information from the diffuse signal that used to be called the 'background'. Rather than fitting the background using arbitrary fitting parameters, as is done in a traditional Rietveld refinement, careful corrections can be made for experimental effects such as Compton scattering, fluorescence, multiple scattering and scattering from sample environments. The resulting 'background' beneath and between the Bragg peaks of the corrected data is information-rich diffuse scattering from the sample, which contains information about the local structure and how it deviates from the average crystal structure in the form of defects and correlated lattice dynamics (phonons). Total-scattering methods that include both the Bragg and diffuse scattering are only now being fully appreciated, with quantitative analyses being carried out in real space using the atomic pair distribution function (PDF) method, and in reciprocal space with Monte Carlo simulated-annealing-type modelling based on the Debye equation.

In this introductory chapter, the basic physics behind the observation of a powder diffraction pattern is described. In accordance with the scheme in Fig. 1.1.1, the information in a powder diffraction pattern can be described by the Bragg-peak positions, the peak profile, the Bragg-peak intensities and the non-Bragg-scattering contributions to the background. After describing the fundamentals of scattering by a crystalline powder, the chapter is organized such that each of the paths illustrated in Fig. 1.1.1 is followed and described in an introductory way. Detailed descriptions of the state of the art in the kinds of studies covered in Fig. 1.1.1 can be found in following chapters, but here we discuss each aspect of powder diffraction in turn, giving a high-level overview of what information is available from powder diffraction as well as explaining the fundamental origin of the features containing that information. We do not attempt to review applications of the different kinds of studies, leaving that to the following chapters.

In this chapter we have drawn heavily on information within three textbooks (Dinnebier & Billinge, 2008; Mittemeijer & Welzel, 2012; Egami & Billinge, 2013) and references therein.

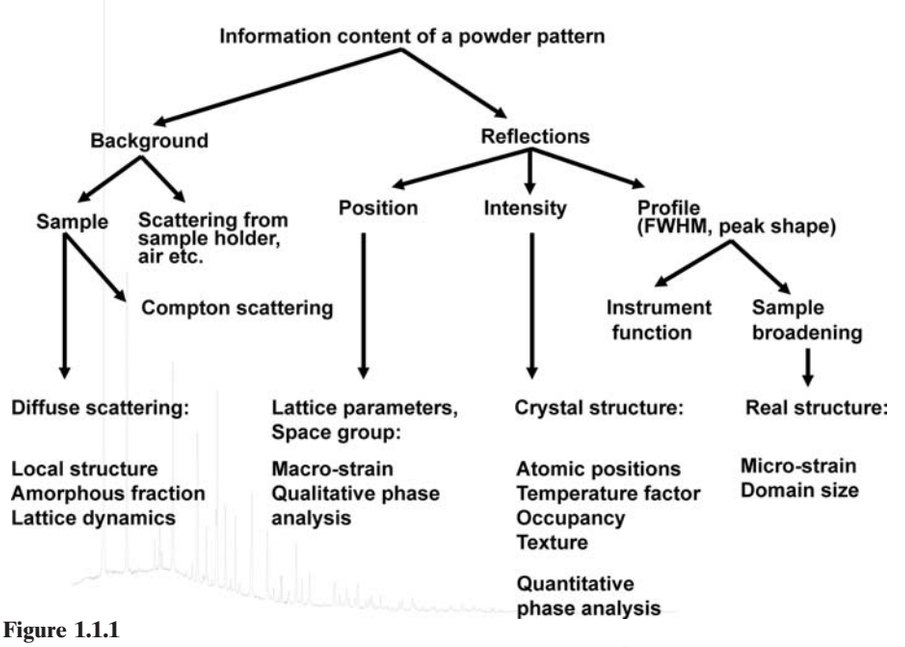

Figure 1.1.1
Schematic picture of the information content of a powder pattern. [Reproduced from Dinnebier & Billinge (2008) with permission from the Royal Society of Chemistry.]

1.1.2. The peak position

1.1.2.1. *The Bragg equation derived*

The easiest way to understand the structural information contained in powder diffraction, and historically one of the first ways in which diffraction was described, is *via* the well known Bragg equation (Bragg, 1913), which describes the principle of X-ray diffraction in terms of the reflection of X-rays by sets of lattice planes.

To understand the concept of a lattice plane, first imagine a three-dimensional periodic lattice of points, for example the corners of an array of cubes stacked in three dimensions. We can imagine a particular plane through the lattice by placing each layer of the stack of cubes on a tray: the tray then defines a lattice plane. Now imagine making the tray thinner and thinner until it

is infinitely thin, but still goes through the same set of points (the cube corners). What we see is that there is not just a single plane, but a series of equivalent planes: for example, between the top and second layers, the second and third layers, and so on. Each plane is parallel to the others and subsequent planes are separated by the same distance (the height of the cube). This is a set of lattice planes. We can also envisage inserting the trays in other ways. For example, we could place the trays vertically rather than horizontally and running from the left side to the right side of the stack of cubes, or alternatively running from the front of the stack to the back of the stack. Each of these is a different set of lattice planes (Fig. 1.1.2), although in this case they have the same layer spacing, or periodicity. If we were able to insert the tray at different angles to the cubes, for example at 45°, we could find other sets of parallel planes that, when we force them to go through some well defined subset of the points defining the lattice, will have well defined layer spacings or periodicities. Bragg's law showed that the diffraction pattern could be understood in terms of X-rays reflecting specularly off subsequent planes in each of these sets of planes and emerging in phase. (In reality, the actual effect is not specular reflection of light from an abstract plane, but a diffraction effect. However, the combination of diffraction and periodicity results in a selection rule that intense scattering only occurs when this particular specular-reflection condition holds.)

There are actually an infinite number of lattice planes in an infinite lattice, and it is important to have a way of labelling them, which is commonly done using the triplet of indices *hkl*, called Miller indices, where h, k and l are integers, and the separation of the planes is denoted by the distance d_{hkl}. When h, k and l have small values the planes are said to be 'low-order' planes. Low-order planes have the largest interplanar separations, and for a particular symmetry of the lattice there is a direct relationship between the Miller indices and d_{hkl}.

The Bragg equation gives the condition that must hold for specular reflection from subsequent planes in a set to be perfectly in phase, as illustrated in Fig. 1.1.3. It is evident in Fig. 1.1.3 that the wave reflecting off the lower plane travels a longer distance (by PN before and NQ after reflection occurs) than the wave reflecting off the upper plane. The two waves are in phase, resulting in constructive interference, only when $\Delta = |\mathrm{PN}| + |\mathrm{NQ}|$ is a multiple $n = 0, 1, 2, \ldots$ of the wavelength λ,

$$\Delta = n\lambda. \tag{1.1.1}$$

In all other cases, destructive interference results, since it is always possible to find a deeper plane, p, for which the relation

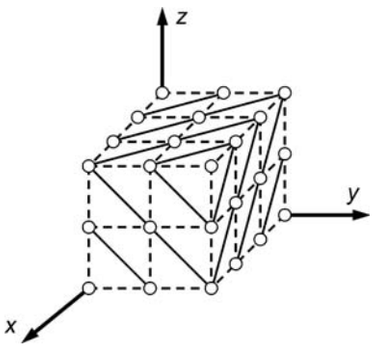

Figure 1.1.2
Schematic drawing of a set of parallel lattice planes (111) passing through all points of the cubic lattice.

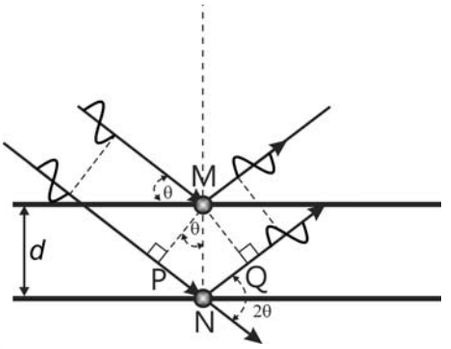

Figure 1.1.3
Illustration of the geometry used for the simplified derivation of Bragg's law. [Reproduced from Dinnebier & Billinge (2008) with permission from the Royal Society of Chemistry.]

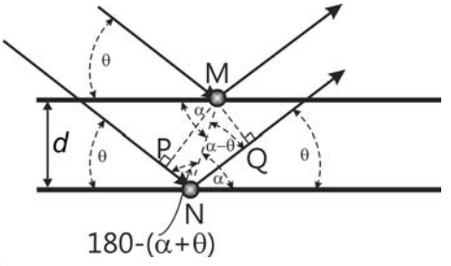

Figure 1.1.4
Illustration of the geometry in the general case where scattering takes place at the position of atoms in consecutive planes. [Reproduced from Dinnebier & Billinge (2008) with permission from the Royal Society of Chemistry.]

$p\Delta = n\lambda + 1/2$ exactly holds, giving rise to perfect destructive interference. Thus, when a narrow beam of X-rays impinges on a crystalline sample, sharp peaks in the intensity of the scattered X-rays are seen only at the angles for which equation (1.1.1) holds, with no intensity observed at other angles. As can easily be seen from Fig. 1.1.3, geometrically,

$$\Delta = 2d\sin\theta, \tag{1.1.2}$$

where d is the interplanar spacing of the parallel lattice planes and 2θ is the diffraction (or 'scattering') angle, the angle between the incoming and outgoing X-ray beams. The angle $\theta = 2\theta/2$ is often called the Bragg angle. Combining equations (1.1.1) and (1.1.2) we get

$$n\lambda = 2d\sin\theta, \tag{1.1.3}$$

which is the Bragg equation (Bragg, 1913).

This simplified derivation of the Bragg equation is often reproduced in textbooks. Although it leads to the correct solution, it has a serious drawback. In reality the X-rays are not reflected by planes, but are scattered by electrons bound to the atoms in the sample. The planes within a crystal are not like shiny optical mirrors, but contain discrete atoms separated by regions of much lower electron density and, in general, the atoms in one plane will not lie exactly above atoms in the plane below as implied by Fig. 1.1.3. How is it then that the simplified picture shown in Fig. 1.1.3 gives the correct result? A more general description shows that equation (1.1.3) is also valid if the atom in the lower lattice plane in Fig. 1.1.3 is shifted by an arbitrary amount within the plane (Fig. 1.1.4).

The phase shift can immediately be deduced from Fig. 1.1.4 as

$$\begin{aligned} n\lambda &= \mathrm{MN}\cos[180^\circ - (\alpha+\theta)] + \mathrm{MN}\cos(\alpha-\theta) \\ &= \mathrm{MN}[-\cos(\alpha+\theta) + \cos(\alpha-\theta)]. \end{aligned} \tag{1.1.4}$$

Using the standard trigonometric results

$$\cos(\alpha+\theta)=\cos\alpha\cos\theta-\sin\alpha\sin\theta,$$
$$\cos(\alpha-\theta)=\cos\alpha\cos\theta+\sin\alpha\sin\theta, \quad (1.1.5)$$

equation (1.1.4) becomes

$$n\lambda=\mathrm{MN}(2\sin\alpha\sin\theta) \quad (1.1.6)$$

with

$$d=\mathrm{MN}\sin\alpha, \quad (1.1.7)$$

which may be substituted to yield the Bragg equation:

$$n\lambda=2d\sin\theta. \quad (1.1.8)$$

The Bragg equation holds for any radiation or particle that is used to probe the structure of the sample: X-rays, neutrons or electrons. Another equivalent, and highly useful, form of the Bragg equation for the particular case of X-rays is

$$Ed=\frac{6.199}{\sin\theta}\ \text{with}\ \lambda=\frac{12.398}{E}, \quad (1.1.9)$$

where the energy E of the X-rays is in keV and λ is in ångströms.

The Bragg law results in narrow beams of high intensity that emerge from the crystal in specific directions given by the Bragg equation, resulting in sharp spots on the detector, and there is a one-to-one correspondence between these Bragg spots (often referred to as Bragg reflections) and each set of crystallographic planes. Each Bragg spot is therefore labelled with the same set of Miller indices, *hkl*, as the set of planes that gave rise to it.

It is possible to construct a 'reciprocal space' where the axes of the space are in units of inverse length. The reference coordinate frame of the reciprocal space is defined by a set of basis vectors whose directions are perpendicular to the plane normals of the (100), (010) and (100) planes of the crystal. Thus, a *point* in this reciprocal space corresponds to a *direction* in direct space and every allowed reflection according to the Bragg law is represented by a point in reciprocal space. The set of points arising from the Bragg law forms a lattice in reciprocal space, which is called the 'reciprocal lattice', and each single crystal has its own reciprocal lattice. [See *International Tables for Crystallography* Volume B (Shmueli, 2008) for more details.]

To derive the Bragg equation, we used an assumption of specular reflection, which is borne out by experiment: for a crystalline material, destructive interference eliminates scattered intensity in all directions except where equation (1.1.3) holds. Strictly this holds only for crystals that are infinite in extent and which the incident X-ray beam can penetrate without loss of intensity. This does not sound like a particularly good approximation, but in practice it holds rather well. Even a fairly low energy X-ray beam that only penetrates, say, a micrometre into the material will still probe ~10 000 atomic layers. The condition is not strictly obeyed in the presence of defects and disorder in the material. In such materials the Bragg peaks are modified in their position, their width and their shape, and there is also an additional component of the diffracted intensity that may be observed in all directions, away from reciprocal-lattice points, known as diffuse scattering.

1.1.2.2. *The Bragg equation from the reciprocal lattice*

Here we develop in more detail the mathematics of the reciprocal lattice. The reciprocal lattice has been adopted by crystallographers as a simple and convenient representation of the physics of diffraction by a crystal. It is an extremely useful tool for describing all kinds of diffraction phenomena occurring in powder diffraction.

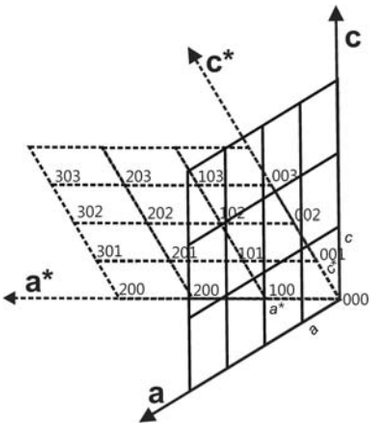

Figure 1.1.5
A two-dimensional monoclinic lattice and its corresponding reciprocal lattice. [Adapted from Dinnebier & Billinge (2008) with permission from the Royal Society of Chemistry.]

Consider a 'normal' crystal lattice with lattice vectors **a**, **b** and **c**, which have lengths a, b and c, respectively, and angles α between **b** and **c**, β between **a** and **c** and γ between **a** and **b**. The unit-cell volume is given by V. A second lattice with lattice parameters a^*, b^*, c^*, α^*, β^*, γ^* and unit-cell volume V^* with the same origin exists such that

$$\mathbf{a}\cdot\mathbf{b}^*=\mathbf{a}\cdot\mathbf{c}^*=\mathbf{b}\cdot\mathbf{c}^*=\mathbf{a}^*\cdot\mathbf{b}=\mathbf{a}^*\cdot\mathbf{c}=\mathbf{b}^*\cdot\mathbf{c}=0,$$
$$\mathbf{a}\cdot\mathbf{a}^*=\mathbf{b}\cdot\mathbf{b}^*=\mathbf{c}\cdot\mathbf{c}^*=1. \quad (1.1.10)$$

This is known as the reciprocal lattice[1] (Fig. 1.1.5), which exists in so-called reciprocal space. As mentioned above, we will see that it turns out that the points in the reciprocal lattice are related to the vectors defining the crystallographic plane normals. There is one point in the reciprocal lattice for each set of crystallographic planes, (*hkl*), separated by distance d_{hkl}, as discussed below. For now, just consider h, k and l to be integers that index a point in the reciprocal lattice. A reciprocal-lattice vector $\mathbf{h}_{hkl}$ is the vector from the origin of reciprocal space to the reciprocal-lattice point for the plane (*hkl*),

$$\mathbf{h}_{hkl}=h\mathbf{a}^*+k\mathbf{b}^*+l\mathbf{c}^*,\quad h,k,l\in\mathbb{Z}. \quad (1.1.11)$$

where $\mathbb{Z}$ is the set of all integers.

The length of the reciprocal basis vector $\mathbf{a}^*$ is defined according to

$$\mathbf{a}^*=x(\mathbf{b}\times\mathbf{c}), \quad (1.1.12)$$

where the scale factor x can easily be deduced, using equations (1.1.12) and (1.1.10), as

$$\mathbf{a}^*\cdot\mathbf{a}=x(\mathbf{b}\times\mathbf{c}\cdot\mathbf{a})=xV\Rightarrow x=\frac{1}{V}, \quad (1.1.13)$$

leading to

$$\mathbf{a}^*=\frac{1}{V}(\mathbf{b}\times\mathbf{c}),\quad \mathbf{b}^*=\frac{1}{V}(\mathbf{c}\times\mathbf{a}),\quad \mathbf{c}^*=\frac{1}{V}(\mathbf{a}\times\mathbf{b}) \quad (1.1.14)$$

and, *vice versa*,

[1] The reciprocal lattice is a commonly used construct in solid-state physics, but with a different normalization: $\mathbf{a}\cdot\mathbf{a}^*=2\pi$.

$$\mathbf{a} = \frac{1}{V^*}(\mathbf{b}^* \times \mathbf{c}^*), \quad \mathbf{b} = \frac{1}{V^*}(\mathbf{c}^* \times \mathbf{a}^*), \quad \mathbf{c} = \frac{1}{V^*}(\mathbf{a}^* \times \mathbf{b}^*). \tag{1.1.15}$$

The relationship between the reciprocal and the real lattice parameters expressed geometrically rather than in the vector formalism used above is

$$\begin{aligned} a^* &= \frac{bc\sin\alpha}{V}, \\ b^* &= \frac{ac\sin\beta}{V}, \\ c^* &= \frac{ab\sin\gamma}{V}, \\ \cos\alpha^* &= \frac{\cos\beta\cos\gamma - \cos\alpha}{\sin\beta\sin\gamma}, \\ \cos\beta^* &= \frac{\cos\alpha\cos\gamma - \cos\beta}{\sin\alpha\sin\gamma}, \\ \cos\gamma^* &= \frac{\cos\alpha\cos\beta - \cos\gamma}{\sin\alpha\sin\beta}, \\ V &= abc\sqrt{1 + 2\cos\alpha\cos\beta\cos\gamma - \cos^2\alpha - \cos^2\beta - \cos^2\gamma}. \end{aligned} \tag{1.1.16}$$

Equation (1.1.16) is the most general expression for non-orthogonal lattices. The expressions simplify considerably for higher-symmetry crystal systems.

We now re-derive Bragg's law using the vector notation introduced above (Fig. 1.1.6). The wave vectors of the incoming and outgoing beams are given by $\mathbf{s}_0$ and $\mathbf{s}$, respectively. They point in the direction of propagation of the wave and their length depends on λ. For elastic scattering (for which there is no change in wavelength on scattering), $\mathbf{s}_0$ and $\mathbf{s}$ have the same length.

We define the scattering vector as

$$\mathbf{h} = (\mathbf{s} - \mathbf{s}_0), \tag{1.1.17}$$

which for a specular reflection is always perpendicular to the scattering plane. The length of $\mathbf{h}$ is given by

$$\frac{h}{s} = 2\sin\theta. \tag{1.1.18}$$

Comparison with the formula for the Bragg equation (1.1.3),

$$\frac{n\lambda}{d} = 2\sin\theta, \tag{1.1.19}$$

gives

$$\frac{n\lambda}{d} = \frac{h}{s}. \tag{1.1.20}$$

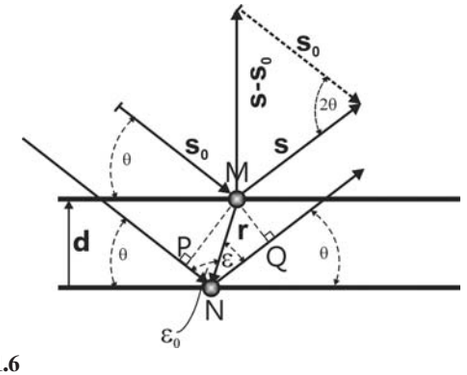

Figure 1.1.6
Illustration of the important wave and scattering vectors in the case of elastic Bragg scattering. [Reproduced from Dinnebier & Billinge (2008) with permission from the Royal Society of Chemistry.]

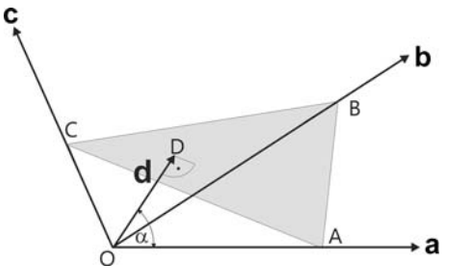

Figure 1.1.7
Geometrical description of a lattice plane in terms of real-space basis vectors. The arc and dot below the letter D indicate a right angle. [Reproduced from Dinnebier & Billinge (2008) with permission from the Royal Society of Chemistry.]

Setting the magnitude of $\mathbf{s}$ to $1/\lambda$, we get the Bragg equation in terms of the magnitude h of the scattering vector,

$$h = \frac{n}{d}. \tag{1.1.21}$$

This shows that diffraction occurs when the magnitude of the scattering vector is an integral number of reciprocal-lattice spacings $1/d$. We define a vector $\mathbf{d}^*$ perpendicular to the lattice planes with length $1/d$. Since $\mathbf{h}$ is perpendicular to the scattering plane, this leads to

$$\mathbf{h} = n\mathbf{d}^*. \tag{1.1.22}$$

Diffraction can occur at different scattering angles 2θ for the same crystallographic plane, giving the different orders n of diffraction. For simplicity, the number n will be incorporated in the indexing of the lattice planes, where

$$d^*_{nh,nk,nl} = nd^*_{hkl}, \tag{1.1.23}$$

e.g., $d^*_{222} = 2d^*_{111}$, and we get an alternative expression for Bragg's equation:

$$\mathbf{h} = \mathbf{d}^*_{hkl}. \tag{1.1.24}$$

The vector $\mathbf{d}^*_{hkl}$ points in a direction perpendicular to a real-space lattice plane. We would like to express this vector in terms of the reciprocal-space basis vectors $\mathbf{a}^*$, $\mathbf{b}^*$, $\mathbf{c}^*$.

First we define $\mathbf{d}_{hkl}$ in terms of the real-space basis vectors $\mathbf{a}$, $\mathbf{b}$, $\mathbf{c}$. Referring to Fig. 1.1.7, we can define

$$\mathbf{OA} = \frac{1}{h}\mathbf{a}, \quad \mathbf{OB} = \frac{1}{k}\mathbf{b}, \quad \mathbf{OC} = \frac{1}{l}\mathbf{c} \tag{1.1.25}$$

with h, k and l being integers, as required by the periodicity of the lattice.

The plane-normal vector $\mathbf{d}_{hkl}$ originates on one plane and terminates on the next parallel plane. Therefore, $\mathbf{OA}\cdot\mathbf{d} = (\mathrm{OA})d\cos\alpha$. From Fig. 1.1.7 we see that, geometrically, $(\mathrm{OA})\cos\alpha = d$. Substituting, we get $\mathbf{OA}\cdot\mathbf{d} = d^2$. Combining this with equation (1.1.25) leads to

$$\frac{1}{h}\mathbf{a}\cdot\mathbf{d} = d^2 \tag{1.1.26}$$

and consequently

$$h = \mathbf{a}\cdot\frac{\mathbf{d}}{d^2}, \quad k = \mathbf{b}\cdot\frac{\mathbf{d}}{d^2}, \quad l = \mathbf{c}\cdot\frac{\mathbf{d}}{d^2}. \tag{1.1.27}$$

By definition, h, k and l are divided by their largest common integer to be Miller indices. The vector $\mathbf{d}^*_{hkl}$, from Bragg's equation (1.1.24), points in the plane-normal direction parallel to $\mathbf{d}$ but with length $1/d$. We can now write $\mathbf{d}^*_{hkl}$ in terms of the

vector **d**:

$$\mathbf{d}^*_{hkl} = \frac{\mathbf{d}}{d^2}, \tag{1.1.28}$$

which gives

$$\mathbf{d}^*_{hkl} = \frac{\mathbf{d}_{hkl}}{d^2} = h\mathbf{a} + k\mathbf{b} + l\mathbf{c}, \tag{1.1.29}$$

or written in terms of the reciprocal basis

$$\mathbf{d}^*_{hkl} = h\mathbf{a}^* + k\mathbf{b}^* + l\mathbf{c}^*, \tag{1.1.30}$$

which was obtained using

$$\begin{aligned}\mathbf{d}^*_{hkl}\cdot\mathbf{a}^* &= h\mathbf{a}\cdot\mathbf{a}^* + k\mathbf{b}\cdot\mathbf{a}^* + l\mathbf{c}\cdot\mathbf{a}^* = h,\\ \mathbf{d}^*_{hkl}\cdot\mathbf{b}^* &= h\mathbf{a}\cdot\mathbf{b}^* + k\mathbf{b}\cdot\mathbf{b}^* + l\mathbf{c}\cdot\mathbf{b}^* = k,\\ \mathbf{d}^*_{hkl}\cdot\mathbf{c}^* &= h\mathbf{a}\cdot\mathbf{c}^* + k\mathbf{b}\cdot\mathbf{c}^* + l\mathbf{c}\cdot\mathbf{c}^* = l.\end{aligned} \tag{1.1.31}$$

Comparing equation (1.1.30) with equation (1.1.11) proves the identity of $\mathbf{d}^*_{hkl}$ and the reciprocal-lattice vector $\mathbf{h}_{hkl}$. Bragg's equation, (1.1.24), can be re-stated as

$$\mathbf{h} = \mathbf{h}_{hkl}. \tag{1.1.32}$$

In other words, diffraction occurs whenever the scattering vector **h** equals a reciprocal-lattice vector $\mathbf{h}_{hkl}$. This powerful result is visualized in the useful Ewald construction, which is described in Section 1.1.2.4.

Useful equivalent variations of the Bragg equation are

$$|\mathbf{h}| = \left|\mathbf{s} - \mathbf{s}_0\right| = \frac{2\sin\theta}{\lambda} = \frac{1}{d} \tag{1.1.33}$$

and

$$|\mathbf{Q}| = \frac{4\pi\sin\theta}{\lambda} = \frac{2\pi}{d}. \tag{1.1.34}$$

The vector **Q** is the physicist's equivalent of the crystallographer's **h**. The physical meaning of **Q** is the momentum transfer on scattering and it differs from the scattering vector **h** by a factor of 2π.

1.1.2.3. *The Bragg equation from the Laue equation*

Another approach for describing scattering from a material was first described by Laue (von Laue, 1912). The Laue equation can be derived by evaluating the phase relation between two wavefronts after hitting two scatterers that are separated by the vector **r**. The path-length difference $\Delta = |\mathrm{CD}| - |\mathrm{BA}|$ between the two scattered waves introduces a phase shift between the two outgoing waves (Fig. 1.1.8). From Fig. 1.1.8 one immediately sees that the path-length difference is given by

$$\Delta = r\cos\varepsilon - r\cos\varepsilon_0. \tag{1.1.35}$$

This path-length difference gives rise to a phase shift

$$\varphi = 2\pi\frac{\Delta}{\lambda} = 2\pi\left(\frac{r}{\lambda}\cos\varepsilon - \frac{r}{\lambda}\cos\varepsilon_0\right). \tag{1.1.36}$$

The term in parentheses is

$$\mathbf{s}\cdot\mathbf{r} - \mathbf{s_0}\cdot\mathbf{r} = (\mathbf{s} - \mathbf{s_0})\cdot\mathbf{r} = \mathbf{h}\cdot\mathbf{r}. \tag{1.1.37}$$

The amplitude of the scattered wave at a large distance away in the direction of the vector **s** is

$$A(\mathbf{h}) = \exp(2\pi i 0) + \exp(2\pi i\mathbf{h}\cdot\mathbf{r}) \tag{1.1.38}$$

When we generalize the idea laid out above to *n* scatterers, we get

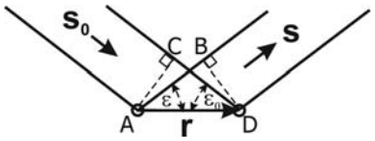

Figure 1.1.8
Scattering from an object consisting of two scatterers separated by **r**.

$$A(\mathbf{h}) = \sum_{j=1}^{n}\exp\left(2\pi i\mathbf{h}\cdot\mathbf{r}_j\right). \tag{1.1.39}$$

For simplicity, consider the case of an infinite one-dimensional crystal of scatterers that are equally spaced by distance a_i. In this case, $r_j = aj$ and

$$A(h) = \sum_{j=-\infty}^{\infty}\exp(2\pi i haj). \tag{1.1.40}$$

Using the definition for a periodic delta function,

$$\lim_{n\to\infty}\sum_{j=-n}^{n}\exp(2\pi i haj) = \sum_{k=-\infty}^{\infty}\delta(k - ha) \tag{1.1.41}$$

and

$$A(h) = \sum_{k=-\infty}^{\infty}\delta(k - ha), \tag{1.1.42}$$

which is a periodic array of delta functions at positions $h = k/a$. This means that sharp peaks of intensity will only appear when this expression holds, which are the reciprocal-lattice points. This is the same result as given by the Bragg equation (1.1.3) in one dimension. Extending to three dimensions, equations (1.1.40) and (1.1.42) become

$$\begin{aligned}A(\mathbf{h}) = &\sum_{j=-\infty}^{\infty}\exp\left(2\pi i(\mathbf{h}\cdot\hat{\mathbf{a}})aj\right)\sum_{k=-\infty}^{\infty}\exp\left(2\pi i(\mathbf{h}\cdot\hat{\mathbf{b}})bk\right)\\ &\times\sum_{l=-\infty}^{\infty}\exp\left(2\pi i(\mathbf{h}\cdot\hat{\mathbf{c}})cl\right),\end{aligned} \tag{1.1.43}$$

where $\hat{\mathbf{a}} = \mathbf{a}/a$, and

$$A(\mathbf{h}) = \sum_{\mu,\nu,\eta=-\infty}^{\infty}\delta[\mu - (\mathbf{h}\cdot\hat{\mathbf{a}})a]\delta[\nu - (\mathbf{h}\cdot\hat{\mathbf{b}})b]\delta[\eta - (\mathbf{h}\cdot\hat{\mathbf{c}})c]. \tag{1.1.44}$$

Equation (1.1.44) has the same meaning in three dimensions, where intensity appears only when all three delta functions are non-zero. This occurs for the conditions

$$\mathbf{h}\cdot\hat{\mathbf{a}} = \frac{\mu}{a},\ \ \mathbf{h}\cdot\hat{\mathbf{b}} = \frac{\nu}{b}\ \text{and}\ \mathbf{h}\cdot\hat{\mathbf{c}} = \frac{\eta}{c}, \tag{1.1.45}$$

where μ, ν and η are integers. From this follows

$$\mathbf{h}\cdot\mathbf{a} = \mu,\ \ \mathbf{h}\cdot\mathbf{b} = \nu\ \text{and}\ \mathbf{h}\cdot\mathbf{c} = \eta. \tag{1.1.46}$$

These conditions are met when

$$\mathbf{h} = \mu\mathbf{a}^* + \nu\mathbf{b}^* + \eta\mathbf{c}^* = \mathbf{d}^*_{\mu\nu\eta}. \tag{1.1.47}$$

This is exactly Bragg's equation in the form given in equation (1.1.30).

For practical purposes including the indexing of powder patterns and refinement of a structural model, given a set of lattice parameters *a*, *b*, *c*, α, β, γ, the positions for all possible reflections *hkl* can be calculated according to

$$\frac{1}{d_{hkl}} = \frac{1}{V}\left\{\left[h^2b^2c^2\sin^2\alpha + k^2a^2c^2\sin^2\beta + l^2a^2b^2\sin^2\gamma + 2hkabc^2(\cos\alpha\cos\beta - \cos\gamma) + 2kla^2bc(\cos\beta\cos\gamma - \cos\alpha) + 2hlab^2c(\cos\alpha\cos\gamma - \cos\beta)\right]\right\}^{1/2}, \quad (1.1.48)$$

for the triclinic case. Equation (1.1.48) simplifies considerably with symmetry to, for example,

$$\frac{1}{d_{hkl}} = \frac{\sqrt{h^2 + k^2 + l^2}}{a} \quad (1.1.49)$$

for the cubic case.

1.1.2.4. *The Ewald construction and Debye–Scherrer cones*

The Bragg equation shows that diffraction occurs when the scattering vector equals a reciprocal-lattice vector. The scattering vector depends on the geometry of the experiment, whereas the reciprocal-lattice vectors are determined by the orientation and the lattice parameters of the crystalline sample. Bragg's law shows the relationship between these vectors in a scattering experiment. Ewald developed a powerful geometric construction that combines these two concepts in an intuitive way (Ewald, 1921). A sphere of radius $1/\lambda$ is drawn following the recipe below. The Bragg equation is satisfied and diffraction occurs whenever a reciprocal-lattice point coincides with the surface of the sphere.

The recipe for constructing Ewald's sphere[2] is as follows (Fig. 1.1.9):

(1) Draw the incident wave vector $\mathbf{s}_0$. This points in the direction of the incident beam and has length $1/\lambda$.
(2) Draw a sphere centred on the tail of this vector with radius $1/\lambda$. The incident wave vector $\mathbf{s}_0$ defines the radius of the sphere. The scattered wave vector $\mathbf{s}$, also of length $1/\lambda$, points in the direction from the sample to the detector. This vector is also drawn starting from the centre of the sphere and also terminates at a point on the surface of the sphere. The scattering vector $\mathbf{h} = \mathbf{s} - \mathbf{s}_0$ completes the triangle from the tip of $\mathbf{s}$ to the tip of $\mathbf{s}_0$, both of which lie on the surface of the sphere. Thus the surface of the sphere defines the locus of points in reciprocal space where the scattering vector in our experiment may possibly lie.
(3) Draw the reciprocal lattice with the origin lying at the tip of $\mathbf{s}_0$.
(4) Find all the places on the surface of the sphere where reciprocal-lattice points lie. This gives the set of points in reciprocal space where the expression $\mathbf{h} = \mathbf{h}_{hkl}$ may possibly be satisfied in our experiment.

This construction places a reciprocal-lattice point at one end of $\mathbf{h}$. The other end of $\mathbf{h}$ lies on the surface of the sphere by definition. Thus, Bragg's law is only satisfied when another reciprocal-lattice point coincides with the surface of the sphere. Diffraction can be envisaged as beams of X-rays emanating from the sample in these directions. In order to detect the intensity of these diffracted beams, one simply moves the detector to the right position. Any vector between two reciprocal-lattice points has the potential to produce a Bragg peak. The Ewald-sphere construction indicates which of these possible reflections are experimentally accessible.

[2] For practical reasons, plots of the Ewald 'sphere' are circular cuts through the sphere and the corresponding slice of reciprocal space.

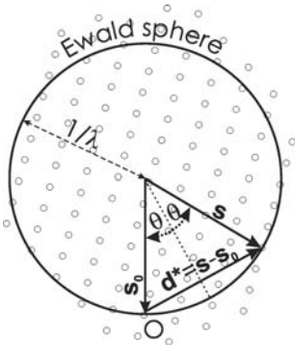

Figure 1.1.9
Simplified representation of the Ewald-sphere construction as a circle in two dimensions. O marks the origin of reciprocal space. The vectors are defined in the text. [Reproduced from Dinnebier & Billinge (2008) with permission from the Royal Society of Chemistry.]

Changing the orientation of the crystal reorients the reciprocal lattice, bringing different reciprocal-lattice points onto the surface of the Ewald sphere. In a single-crystal experiment it is necessary to repeatedly reorient the crystal to bring new reciprocal-lattice points onto the surface of the Ewald sphere, and then to reorient the detector in such a way as to measure the scattering from each particular reflection on the surface. This is done in a highly automated fashion these days. Once a diffraction pattern has been indexed so that the lattice vectors and the orientation matrix (the relation of the lattice vectors to the laboratory coordinate frame) are found, then all of the diffractometer settings that are required to collect all the Bragg peaks are fully determined and this process can be accomplished automatically.

In this chapter we are considering scattering from powders. An ideal powder contains individual crystallites in all possible orientations with equal probability. The powder experiment is equivalent to placing a detector at a fixed position and rotating a single crystal through every orientation, spending an equal amount of time in each orientation. The first powder experiment was reported by Debye & Scherrer in 1916, and independently by Hull in 1917. In the Ewald construction, this is the same as

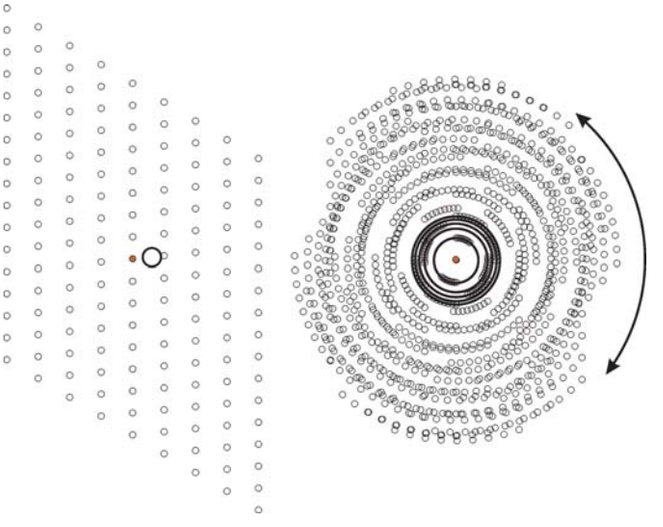

Figure 1.1.10
Illustration of the reciprocal lattice associated with a single-crystal lattice (left) and a large number of randomly oriented crystallites (right). A real powder consists of so many grains that the dots of the reciprocal lattice form into continuous lines. [Reproduced from Dinnebier & Billinge (2008) with permission from the Royal Society of Chemistry.]

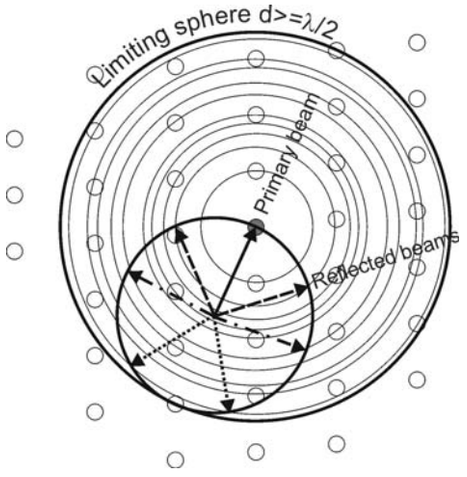

Figure 1.1.11
Simplified representation of the Ewald-sphere construction as a circle in two dimensions. Illustration of the region of reciprocal space that is accessible in a powder diffraction experiment. The smaller circle represents the Ewald sphere. As shown in Fig. 1.1.10, a powder sample has crystallites in all possible orientations, which is modelled by rotating the reciprocal lattice to sample all orientations. An equivalent operation is to rotate the Ewald sphere in all possible orientations around the origin of reciprocal space. The volume swept out is the region of reciprocal space accessible in the experiment. [Reproduced from Dinnebier & Billinge (2008) with permission from the Royal Society of Chemistry.]

smearing out every reciprocal-lattice point over the surface of a sphere centred on the origin of reciprocal space. This is illustrated in Fig. 1.1.10. The orientation of the $\mathbf{d}^*_{hkl}$ vector is lost and the three-dimensional vector space is reduced to one dimension with the independent variable being the modulus of the vector $\left|\mathbf{d}^*_{hkl}\right| = 1/d$.

These spherical shells intersect the surface of the Ewald sphere in circles. A two-dimensional projection is shown in Fig. 1.1.11. Diffracted beams can be envisaged as emanating from the sample in, and only in, the directions where the thin circles from the smeared reciprocal lattice intersect the thick circle of the Ewald sphere. A few representative diffraction beams are indicated by the dashed, dotted and dash-dotted arrows.

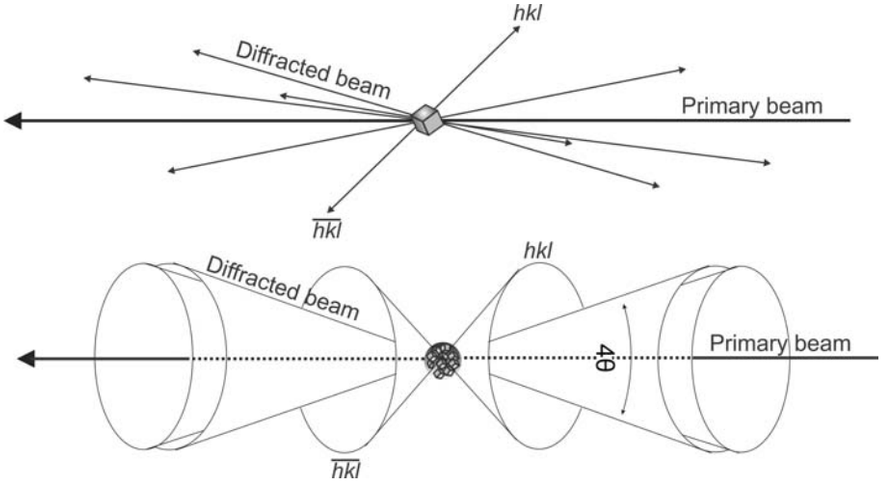

Figure 1.1.12
Comparison between the scattered beams originating from a single crystal (top) and a powder (bottom). For the latter, some Debye–Scherrer cones are drawn in reciprocal space. [Reproduced from Dinnebier & Billinge (2008) with permission from the Royal Society of Chemistry.]

The reflections from planes with the smallest d-spacing that are accessible in the experiment are determined by the diameter of the Ewald sphere, which is $2/\lambda$. In order to increase the number of reflections that can be detected, one must decrease the incident wavelength. In the case of an energy-dispersive experiment such as a time-of-flight neutron powder diffraction experiment, which makes use of a continuous distribution of wavelengths from λ_{min} to λ_{max} at fixed angle, all reflections that lie in the cone-shaped region of reciprocal space between the two limiting Ewald spheres at $2/\lambda_{min}$ and $2/\lambda_{max}$ will be detected.

As mentioned above, in a powder the reciprocal-lattice points get smeared into a spherical surface, which intersects the Ewald sphere as a circle. This means that, in three dimensions, the resulting diffracted radiation associated with the reflection *hkl* forms a cone emanating from the sample on an axis given by the direct beam, the so-called Debye–Scherrer cone. Different reciprocal-lattice points, at different values of $1/d_{hkl}$, give rise to coaxial cones of scattering. This is illustrated in Fig. 1.1.12.

The smearing of reciprocal space in a powder experiment makes the measurement of a powder diffraction pattern easier than the measurement of a set of single-crystal data, because the sample does not have to be repeatedly re-oriented, but this comes at the cost of a loss of information. At first sight the loss of information seems to be the directional information about the points in the reciprocal lattice. However, once the lattice is indexed (*i.e.* its basis vectors are known) the directional information in the pattern can be recovered without difficulty, which is why three-dimensional structures can be determined from the one-dimensional diffraction information in a powder pattern. The loss of information comes from the fact that reflections from lattice planes whose vectors lie in different directions but which have the same d-spacing overlap. These reflections cannot be resolved by the measurement and so the intensity in each of the peaks is not known. The peak-overlap problem becomes increasingly worse with increasing scattering angle as the number of diffraction planes in a particular d-spacing range increases and their separation decreases.

Some of these overlaps are dictated by symmetry (systematic overlaps) and others are accidental. Systematic overlaps are less problematic because the number of equivalent reflections (the multiplicity) is known from the symmetry, and, by symmetry, each of the overlapping peaks has the same intensity. For highly crystalline samples, the number of accidental overlaps can be reduced by making measurements with higher resolution, since this allows similar but not identical d-spacings to be separated.

To obtain the maximum amount of information, a spherical-shell detector would be desirable, although this is currently impractical. Often, a flat two-dimensional detector, either film, an image plate or a charge-coupled device (CCD), is placed perpendicular to the direct beam, or offset to one side to increase the angular range of the data collected. In this case, the Debye–Scherrer cones appear as circles, as shown in Fig. 1.1.13, or as ellipses if the detector is at an angle to the direct beam.

For an ideal powder, the intensity distribution around the rings is uniform. In a traditional powder diffraction experiment using a point detector, for example a scin-

tillator detector behind a receiving slit that defines the angular resolution of the measurement, at each position the detector samples a point on the two-dimensional diffraction pattern shown in Fig. 1.1.13. As the detector is moved to higher 2θ angles the locus of the points that are sampled is a horizontal or vertical (depending on whether the detector is moving in the horizontal or the vertical plane) line across the two-dimensional image. The intensity that is detected is low except where the detector crosses the circles of high intensity. This type of measurement is preferred for obtaining the highest resolution, especially if a highly perfect analyser crystal is used instead of a slit for defining the angle of the scattered beam. However, if the full rings, or fractions of them, are detected with two-dimensional detectors, the counting statistics can be improved enormously by integrating azimuthally around the rings at constant $|\mathbf{h}|$. This mode is becoming very popular for time-resolved, *in situ* and parametric studies where rapid throughput is more important than high resolution. It is also useful for samples that are weakly scattering and for nanometre-sized crystals or defective crystals, which may not show sharper peaks even when measured at higher resolution.

If the powder is non-ideal, the intensity distribution around the ring is no longer uniform, as illustrated in the right part of Fig. 1.1.13, and a one-dimensional scan will give arbitrary intensities for the reflections. To check for this in a conventional measurement it is possible to measure a rocking curve by keeping the detector positioned so that the Bragg condition for a reflection is satisfied and then taking measurements while the sample is rotated. If the powder is ideal, *i.e.* it is uniform and fine-grained enough to sample every orientation uniformly, this will result in a constant intensity as a function of sample angle, while large fluctuations in intensity will suggest a poor powder average. To improve powder statistics, powder samples may be rotated during a single measurement exposure, both for conventional point measurements and for measurements with two-dimensional detectors. Additional averaging of the signal also occurs during the azimuthal integration in the case of two-dimensional detectors. Outlier intensities can be identified and excluded from the integration. On the other hand, the intensity variation around the rings can give important information about the sample, such as preferred orientation of the crystallites or texture.

The *d*-spacings that are calculated from a powder diffraction pattern will include measurement errors, and it is important to minimize these as much as possible. These can come from uncertainty in the position of the sample, the zero point of 2θ, the angle of the detector or the angle of a pixel on a two-dimensional detector, uncertainties in the wavelength and so on. These effects will be dealt with in detail in later chapters. These aberrations often have a well defined angular dependence which can be included in fits to the data so that the correct underlying Bragg-peak positions can be determined with high accuracy.

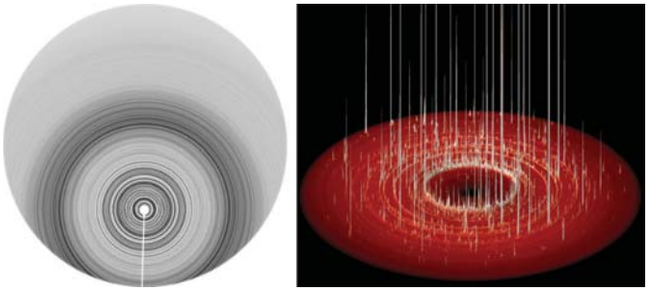

Figure 1.1.13
Left: Debye–Scherrer rings from an ideal fine-grained powder sample of a protein (courtesy Bob Von Dreele). Right: perspective view of Debye–Scherrer rings from a grainy powder sample of $BiBO_3$ at high pressure in a diamond anvil cell.

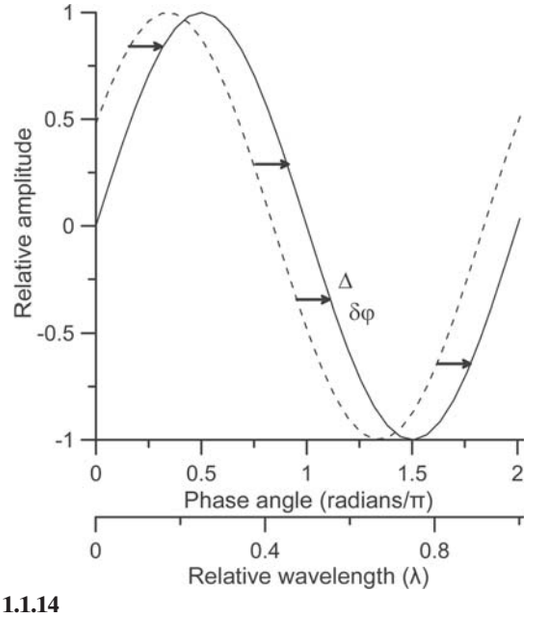

Figure 1.1.14
Graphical illustration of the phase shift between two sine waves of equal amplitude. [Reproduced from Dinnebier & Billinge (2008) with permission from the Royal Society of Chemistry.]

1.1.3. The peak intensity

1.1.3.1. *Adding phase-shifted amplitudes*

Bragg's law gives the *positions* at which diffraction by a crystal will lead to sharp peaks (known as Bragg peaks) in diffracted intensity. We now want to investigate the factors that determine the intensities of these peaks.

X-rays are electromagnetic (EM) waves with a much shorter wavelength than visible light, typically of the order of 1 Å (= 10^{-10} m). The physics of EM waves is well understood and excellent introductions to the subject are found in every textbook on optics. Here we briefly review the results that are most important in understanding the intensities of Bragg peaks.

Classical EM waves can be described by a sine wave of wavelength λ that repeats every 2π radians. If two identical waves are not coincident, they are said to have a phase shift, which is either measured as a shift, Δ, on a length scale in units of the wavelength, or equivalently as a shift in the phase, $\delta\varphi$, on an angular scale, such that

$$\frac{\Delta}{\lambda} = \frac{\delta\varphi}{2\pi} \Rightarrow \delta\varphi = \frac{2\pi}{\lambda}\Delta. \qquad (1.1.50)$$

This is shown in Fig. 1.1.14.

The detected intensity, I, is proportional to the square of the amplitude, A, of the sine wave. With two waves present that are coherent and can interfere, the amplitude of the resultant wave is not just the sum of the individual amplitudes, but depends on the phase shift $\delta\varphi$. The two extremes occur when $\delta\varphi = 0$ (constructive interference), where $I \simeq (A_1 + A_2)^2$, and $\delta\varphi = \pi$ (destructive interference), where $I \simeq (A_1 - A_2)^2$. In general, $I \simeq \left[A_1 + A_2 \exp(i\delta\varphi)\right]^2$. When more than two waves are present, this equation becomes

$$I \simeq \left[\sum_j A_j \exp\left(i\varphi_j\right)\right]^2, \tag{1.1.51}$$

where the sum is over all the sine waves present and the phases, φ_j, are measured with respect to some origin.

Measuring X-ray diffraction involves the measurement of the intensity of X-rays scattered from electrons bound to atoms. Waves scattered by atoms at different positions arrive at the detector with a relative phase shift. Therefore, the measured intensities yield information about the relative atomic positions.

In the case of X-ray diffraction, the Fraunhofer approximation is valid. This is a far-field approximation, where the distances L_1 from the source to the place where scattering occurs (the sample) and L_2 from the sample to the detector are much larger than the separation, D, of the scatterers. This is an excellent approximation, since in this case $D/L_1 \simeq D/L_2 \simeq 10^{-10}$. The Fraunhofer approximation greatly simplifies the mathematics. The incident X-rays come from a distant source and form a wavefront of constant phase that is a plane wave. X-rays scattered by single electrons are outgoing spherical waves, which again appear as plane waves in the far field. This allows us to express the intensity of the diffracted X-rays using equations (1.1.51) and (1.1.39).

This is the origin of equation (1.1.39), which gives the amplitude of the scattered radiation in terms of the scattering vector, $\mathbf{h} = \mathbf{s}_0 - \mathbf{s}$, and the atomic positions, $\mathbf{r}_j$. In fact, the amplitude of the scattered radiation is only proportional to this expression. The actual intensity depends on the amplitude of the incident wave and also on the absolute scattering power of the scatterers. If we neglect for now the incident intensity and assume that our measured intensities are normalized to the incident beam intensity, we get

$$A(\mathbf{h}) = \sum_{j=1}^{n} f_j(h) \exp\left(2\pi i \mathbf{h}\cdot\mathbf{r}_j\right), \tag{1.1.52}$$

where $f_j(h)$ is the atomic form factor and $h = |\mathbf{h}|$ is the magnitude of the scattering vector, and is described in more detail in *International Tables for Crystallography*, Volume C, Part 6. This is a measure of the strength of scattering from the jth atom. At $h = 0$, scattering is in the forward direction with all electrons scattering in phase. As a result, $f_j(0)$ equals the number of electrons bound to the atom (in units of the Thomson scattering cross section for an electron), usually taken to be the atomic number of the atomic species at the jth site. An additional h-dependent reduction of the amplitude comes from positional disorder of the atoms. A Gaussian blurring is used with a width that is often falsely called the 'temperature factor', but is more correctly known as the atomic displacement parameter (ADP). The Gaussian is known as the Debye–Waller factor, which is discussed below. More information can be found in Chapter 4.7.

The crystal structure consists of periodic arrangements of atoms. The simplest structures have one atom in a periodically repeated unit cell. However, in general, there is a well defined group of atoms that forms a structural motif that is periodically repeated. This motif can range from one atom to thousands of atoms in complex protein structures. Solving the crystal structure consists of finding the unit-cell parameters and determining the positions in the unit cell of the atoms in the structural motif. In this sense, the structure of the infinite crystal can be thought of mathematically as a convolution of the periodic lattice that we discussed above with the structural motif. This results in a perfect, orientationally ordered copy of the structural motif in every unit cell translated in three-dimensional space.

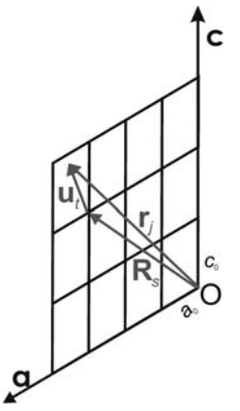

Figure 1.1.15
The position vector of the jth atom $\mathbf{r}_j$ can be decomposed into a vector $\mathbf{R}_s$ from the origin of the crystal to the origin of the unit cell containing the jth atom, and the vector $\mathbf{u}_t$ from the unit cell origin to the jth atom.

As we discussed above, the direct-space lattice has a reciprocal lattice associated with it which determines the positions of the Bragg peaks, or allowed delta functions of scattered intensity. The reciprocal lattice is actually a Fourier transform of the periodic lattice in direct space. The convolution theorem of Fourier transforms tells us that a convolution of two functions in direct space will result in a product of the Fourier transforms of those functions in the Fourier space. Since the structure is a convolution of the direct-space lattice with the structural motif, the reciprocal lattice will be *multiplied* by the Fourier transform of the structural motif. This Fourier transform of the structural motif is called the crystallographic structure factor, F_{hkl}.

This result can be readily derived from equation (1.1.52). In this equation $\mathbf{r}_j$ is the vector from the (arbitrary but fixed) origin to the jth atom in the material. If we now think of the crystal as consisting of n identical cells, each containing an identical structural motif consisting of m atoms, we can write $\mathbf{r}_j$ as a sum of two vectors: a vector that goes from the origin to the corner of the sth unit cell that contains the jth atom, and a second vector that goes from the corner of the sth cell to the position of the jth atom. This is illustrated in Fig. 1.1.15.

Equation (1.1.52) can then be written as

$$A(\mathbf{h}) = \sum_{s=1}^{n}\sum_{t=1}^{m} f_t(h) \exp\left(2\pi i \mathbf{h}\cdot(\mathbf{R}_s + \mathbf{u}_t)\right), \tag{1.1.53}$$

where it is readily seen that the first sum is taken over all the cells in the crystal and the second sum is taken over the m atoms in the structural motif. The equation is readily factored as follows:

$$A(\mathbf{h}) = \sum_{s=1}^{n} \exp(2\pi i \mathbf{h}\cdot\mathbf{R}_s) \sum_{t=1}^{m} f_t(h) \exp(2\pi i \mathbf{h}\cdot\mathbf{u}_t). \tag{1.1.54}$$

Taking n to infinity, we immediately recognise the first sum as the lattice sum of equation (1.1.43), and we can therefore rewrite equation (1.1.54) as

$$\begin{aligned} A(\mathbf{h}) &= \sum_{t=1}^{m} f_t(h) \exp(2\pi i \mathbf{h}\cdot\mathbf{u}_t) \\ &\quad \times \sum_{\mu,\nu,\eta=-\infty}^{\infty} \delta\left[\mu - (\mathbf{h}\cdot\hat{\mathbf{a}})a\right]\delta\left[\nu - (\mathbf{h}\cdot\hat{\mathbf{b}})b\right]\delta\left[\eta - (\mathbf{h}\cdot\hat{\mathbf{c}})c\right], \\ A(\mathbf{h}) &= F_{hkl} \sum_{\mu,\nu,\eta=-\infty}^{\infty} \delta\left[\mu - (\mathbf{h}\cdot\hat{\mathbf{a}})a\right]\delta\left[\nu - (\mathbf{h}\cdot\hat{\mathbf{b}})b\right]\delta\left[\eta - (\mathbf{h}\cdot\hat{\mathbf{c}})c\right]. \end{aligned} \tag{1.1.55}$$

The delta functions determine the positions of the reciprocal-

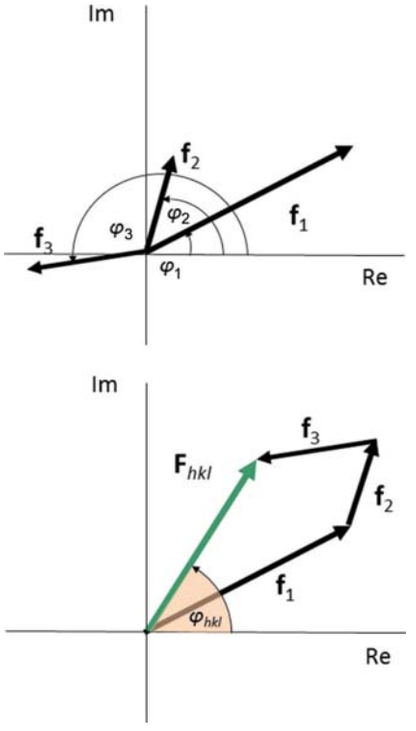

Figure 1.1.16
Graphical illustration of the summation of scattered wave amplitudes $\mathbf{f}_t$ in the complex plane, accounting for the phase shifts coming from the different positions of the atoms in the unit cell.

lattice points (directions of the Bragg peaks), and their intensities are multiplied by a factor, the crystallographic structure factor,

$$F_{hkl} = \sum_{t=1}^{m} f_t(h) \exp(2\pi i \mathbf{h} \cdot \mathbf{u}_t). \qquad (1.1.56)$$

If we write each term as a complex number denoted $\mathbf{f}_t$, we can represent this complex sum as a vector sum in the complex plane, as illustrated in Fig. 1.1.16, where the $\varphi_t = 2\pi \mathbf{h} \cdot \mathbf{u}_t$. The intensity of the Bragg peak depends only on the length of the $\mathbf{F}_{hkl}$, not its direction. However, its length depends on both the lengths *and the phases* of each contribution, which in turn depend on the positions of the atoms within the unit cell. This is the phase information that is 'lost' in a diffraction experiment. Given a structure, we can directly calculate all the Bragg-peak intensities (the 'forward problem'). However, given all the Bragg-peak intensities, we cannot directly calculate the structure (the 'inverse problem'). Structure determination uses the measured intensities and reconstructs the lost phase information using various iterative methods and algorithms.

In fact, the intensity of a Bragg reflection *hkl* is given by the squared absolute value of the structure-factor amplitude F_{hkl},

$$\left|F_{hkl}\right|^2 = \sum_{t,t'=1}^{m} f_t(h) f_{t'}^*(h) \exp\left(2\pi i \mathbf{h} \cdot (\mathbf{u}_t - \mathbf{u}_{t'})\right), \qquad (1.1.57)$$

where * indicates the complex conjugate. This analysis shows that the *positions* of the Bragg peaks determine the geometry of the periodic lattice (the size and shape of the unit cell, for example), but the *intensities* of the Bragg peaks are determined by the relative positions of atoms within the unit cell, scaled by their respective scattering power. To solve the internal structure of the structural motif within the unit cell, it is necessary to measure quantitatively the intensities of many Bragg peaks and use some kind of iterative procedure to move the atoms within the cell until the calculated structure factors self-consistently reproduce the intensities of all the measured Bragg peaks.

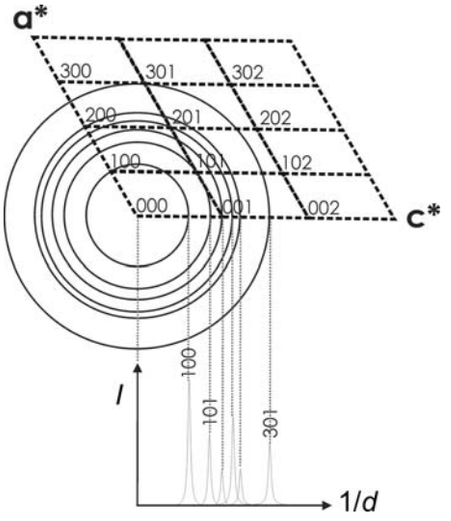

Figure 1.1.17
Schematic illustration of the projection of the reciprocal **a***c* plane (representing the three-dimensional reciprocal-lattice space) into the one-dimensional powder pattern.

The situation is not fundamentally different in a powder diffraction experiment from the single-crystal case, except that the Bragg peaks in three-dimensional reciprocal space are projected into one dimension, as shown in Fig. 1.1.17.

'Indexing' is the term used for deriving the lattice parameters from the positions of the Bragg peaks (see Chapter 3.4). Once the size and shape of the reciprocal lattice is determined, Miller indices can be assigned to each of the Bragg peaks in a one-dimensional powder pattern. If it is possible to extract the intensities of those peaks from the pattern, diffraction data from a powder can be used to reconstruct the three-dimensional structure in exactly the same way as is done with data from a single crystal. This process is known as structure solution from powder diffraction, and is often successful, although it is less well automated than structure solution from data from single crystals. As mentioned above, the main problem with powder data is a loss of information due to systematic and accidental peak overlap, but this can often be overcome.

There are various methods for extracting quantitative peak intensities from indexed powder patterns by computer fitting of profiles to the Bragg peaks at their known positions. Two of the most common are Pawley refinement (Pawley, 1981) and Le Bail refinement (Le Bail *et al.*, 1988), as discussed in Chapter 3.5.

In general, the intensities of the Bragg reflections must be corrected by the product K_{hkl} of various correction factors. Some common correction factors are given by

$$K_{hkl} = M_{hkl} \mathrm{Abs}_{hkl} \mathrm{Ext}_{hkl} \mathrm{LP}_{hkl} \mathrm{PO}_{hkl} \ldots, \qquad (1.1.58)$$

where M_{hkl} is the multiplicity, Abs_{hkl} is an absorption correction, Ext_{hkl} is an extinction correction, LP_{hkl} is the geometrical Lorentz–polarization correction and PO_{hkl} is a correction for preferred orientation (see Chapter 4.7).

If there is more than one crystalline phase present in the sample, and the structures of all the crystalline phases are known, then we can find a scale factor for each phase in the mixture which reproduces the data. This is then a way of determining the proportion of each phase in the sample. This is called quantitative phase analysis (see Chapter 3.9).

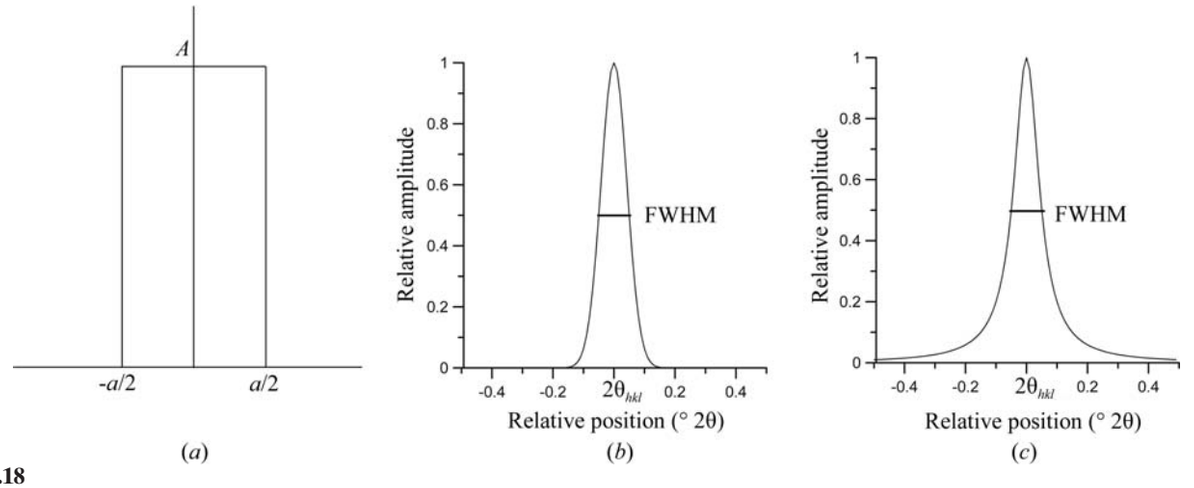

Figure 1.1.18
Normalized peak-shape functions. (*a*) The hat function, (*b*) the Gaussian function and (*c*) the Lorentzian function.

1.1.4. The peak profile

The peak profile refers to the shape of the measured Bragg peak. In the treatment above, the Bragg peaks from a perfect infinite crystal were delta functions and therefore infinitely narrow. In reality, the finite size of the crystal, the finite resolution of the measurement and defects in the material that result in inhomogeneous strains all broaden the delta function, giving it a finite width and some characteristic shape. When fitting a model to the measured diffraction pattern we should correctly account for these effects in order to obtain correct values for the Bragg-peak intensities. On the other hand, a careful study of the peak shapes yields important information about the size of the crystallites in the sample and defects that they contain. With recent improvements in instrumentation and computational data-analysis methods, this latter type of study has become more important and is having considerable scientific and technological impact.

The convolution theorem of the Fourier transform that was introduced in the derivation of the crystallographic structure factor above is also very useful in understanding the peak profile. In this case, the measured Bragg peak can be thought of as a delta function convoluted with a profile (Klug & Alexander, 1974). The profile of the Bragg reflection *hkl*, Φ_{hkl}, can be written as

$$\Phi_{hkl}(2\theta_i - 2\theta_{hkl}) = \mathrm{EP}(2\theta_i) \otimes \mathrm{IP}(2\theta_i) \otimes \mathrm{MS}(2\theta_i - 2\theta_{hkl}), \tag{1.1.59}$$

where $\mathrm{EP}(2\theta_i)$ is the emission profile of the X-ray source (tube or synchrotron), $\mathrm{IP}(2\theta_i)$ contains additional contributions to the profile from the instrument and $\mathrm{MS}(2\theta_i - 2\theta_{hkl})$ is the contribution from the microstructure of the sample. The symbol $\otimes$ denotes convolution.

The convolution of two functions $f(t)$ and $g(t)$ in real space is defined as

$$(f \otimes g)(t) = \int_{\tau=-\infty}^{\infty} f(\tau) g(t-\tau)\, \mathrm{d}\tau. \tag{1.1.60}$$

The convolution theorem tells us that the Fourier transform (FT) of two convoluted functions is the product of the Fourier transforms of those functions:

$$\mathrm{FT}(f \otimes g)(t) = \big(\mathrm{FT}(f)\big)\big(\mathrm{FT}(g)\big). \tag{1.1.61}$$

Normalization of the transform leads to scaling factors like 2π which have been omitted here for simplicity.

In practice, numerical integrations are almost always required, as many of the instrument aberration functions cannot be convoluted analytically. This convolution approach is the basis of the so-called fundamental-parameter (FP) approach (Cheary & Coelho, 1992) and has proven to be superior to other more empirical or phenomenological methods. The idea behind the FP approach is to build up the profile from first principles, exclusively using measurable physical quantities like slit widths, slit lengths, Soller-slit opening angles *etc*. The process of convolution from a fundamental-parameters perspective is an approximation whereby second- and higher-order effects are typically neglected for computational speed and simplicity. The instrumental profile is usually fully characterized by measuring a line-profile standard such as NIST SRM 660c LaB_6, which is expected to contain only small microstructural contributions, and comparing the calculated diffraction pattern to the measured one. Once the instrumental part of the profile is sufficiently well determined, it can be assumed that the remaining contributions to the 'real' profile are purely sample dependent (*e.g.* domain size, strain).

In general, it is desirable to keep the number of functions that are used to describe the peak profile to a minimum. Typical examples of mathematical functions which are convoluted to form the profile of a Bragg reflection include:

(*a*) the hat function H (*e.g.* for all kinds of rectangular slits),

$$H(2\theta - 2\theta_{hkl}) = \begin{cases} A \text{ for } -a/2 < (2\theta - 2\theta_{hkl}) < a/2, \\ 0 \text{ for } (2\theta - 2\theta_{hkl}) \le -a/2 \\ \quad \text{and } (2\theta - 2\theta_{hkl}) \ge -a/2 \end{cases} \tag{1.1.62}$$

(Fig. 1.1.18*a*);

(*b*) the normalized Gaussian G (*e.g.* for microstrain broadening),

$$G(2\theta - 2\theta_{hkl}) = \left(\frac{2\sqrt{\ln(2)/\pi}}{\mathrm{FWHM}}\right) \exp\left(\frac{-4\ln(2)(2\theta - 2\theta_{hkl})^2}{\mathrm{FWHM}^2}\right), \tag{1.1.63}$$

(Fig. 1.1.18*b*), where FWHM denotes the full width at half maximum of the Gaussian function in ° 2θ; and

(*c*) the Lorentzian function L (*e.g.* for the emission profile),

$$L(2\theta - 2\theta_{hkl}) = \frac{1}{2\pi}\left(\frac{\mathrm{FWHM}}{(2\theta - 2\theta_{hkl}) + \mathrm{FWHM}^2/4}\right), \tag{1.1.64}$$

(Fig. 1.1.18*c*).

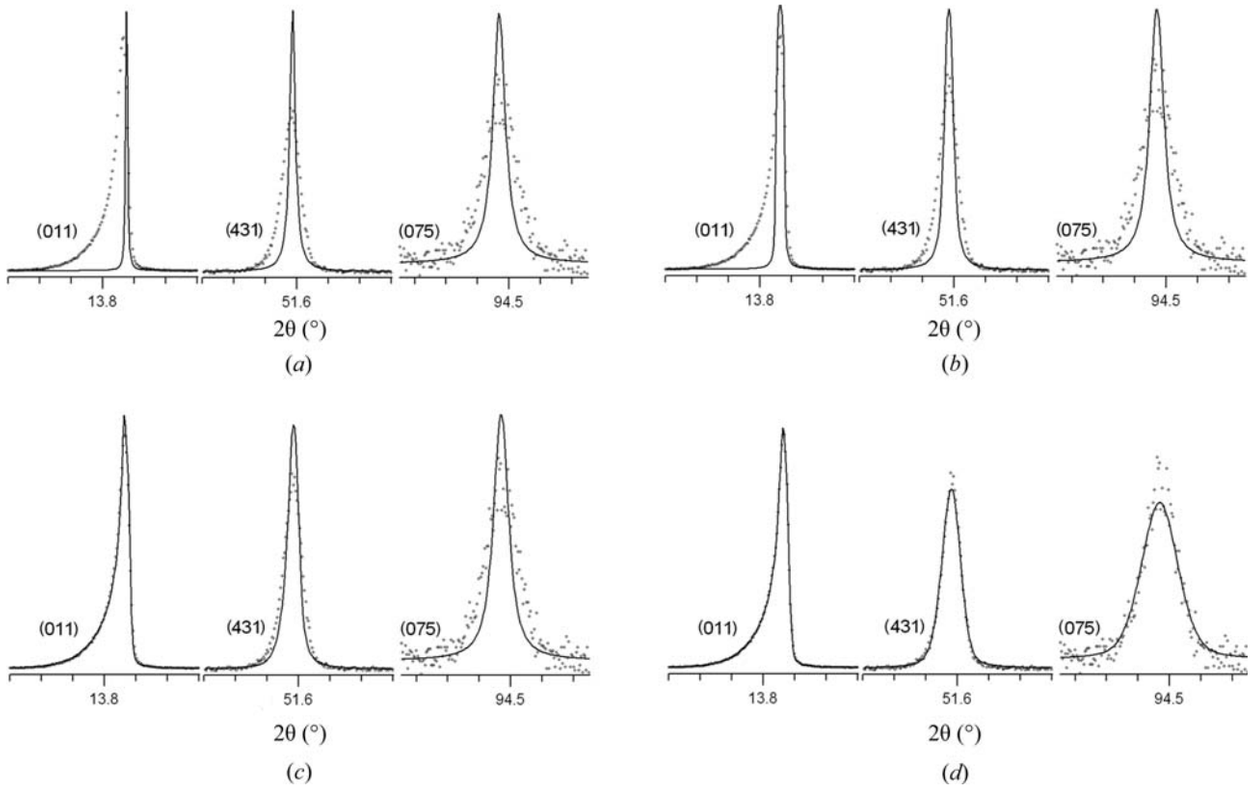

Figure 1.1.19
Peak fits of three selected reflections for an LaB_6 standard measured with Mo $K\alpha_1$ radiation ($\lambda = 0.7093$ Å) from a Ge(220) monochromator in Debye–Scherrer geometry using the fundamental-parameter approach. (*a*) A pure Lorentzian emission profile with a half width of 0.2695 mÅ is applied, refining the peak position and intensity only; (*b*) additionally, a hat shape function of the receiving slit in the equatorial plane with a width of 0.1 mm has been convoluted into the profile; (*c*) additionally, an axial convolution with filament-, sample- and receiving-slit lengths of 8 mm each and a secondary Soller slit with an opening angle of 2.5° has been convoluted into the profile; (*d*) additionally a small contribution of Gaussian broadening coming from the position-sensitive detector is convoluted into the profile. [From Mittemeijer & Welzel (2012). Copyright Wiley-VCH Verlag GmbH & Co. KGaA. Reproduced with permission.]

These functions can be convoluted sequentially as needed, first with the delta-function Bragg peak, and subsequently with the existing profile from the previous convolutions, each time resulting in a new profile that can become quite complex (Fig. 1.1.19). It is often the case that for a particular resolution effect the angular dependence of the profile function is known from the geometry of the measurement, and the convolution function for each peak is determined with only a very small number of parameters.

1.1.4.1. *Sample contributions to the peak profile*

Features of the sample that affect the peak profile include crystallite domain size and shape, dislocations, disclinations, twin and stacking faults, antiphase domains, microstrains, grain surface relaxations, and compositional fluctuations. Here we reproduce some basic results as examples; they also illustrate some fundamental aspects of diffraction from real crystals.

1.1.4.1.1. *Crystallite size*

The starting point for the analysis of finite size effects is the Laue equation, equation (1.1.39), which is reproduced here for a one-dimensional crystal:

$$A(h) = \sum_{j=0}^{n} \exp(2\pi i a j h). \tag{1.1.65}$$

When we were deriving the Bragg equation from the Laue equation we assumed an infinite crystal, and the sum taken to infinity resulted in delta functions at the reciprocal-lattice points. Now we want to consider a finite crystal with n unit cells. There is an analytic form for this sum which, using Euler's identity, is given by

$$\begin{aligned} A(h) &= \frac{\exp\left(2\pi i(n+1)ah\right) - 1}{\exp(2\pi i a h) - 1} \\ &= \frac{\exp\left(i\pi(n+1)ah\right)}{\exp(i\pi a h)} \frac{\exp\left(i\pi(n+1)ah\right) - \exp\left(-i\pi(n+1)ah\right)}{\exp(i\pi a h) - \exp(-i\pi a h)} \\ &= \exp(i\pi n a h) \frac{\sin\left(\pi(n+1)ah\right)}{\sin(\pi a h)}. \end{aligned} \tag{1.1.66}$$

The intensity is obtained by taking the modulus squared of this complex function, resulting in

$$I(h) = \frac{\sin^2\left(\pi(n+1)ah\right)}{\sin^2(\pi a h)}. \tag{1.1.67}$$

This function has sharp maxima when $h = \nu(1/a)$, where ν is an integer. This large central maximum falls off with a width proportional to $1/n^2$ with oscillating tails of intensity where the frequency of the oscillations increases with increasing n. This is illustrated in Fig. 1.1.20 for two different values of n but the same value of a.

In general, the Fourier transforms of periodic patterns become sharper with increasing number of unit cells. The expression $\sin(\pi(n+1)ah)/\sin(\pi a h)$ is also called the geometric factor of the structure amplitude.

This size broadening is often modelled in practice by using an equation due to Scherrer. We now reproduce the simple deri-

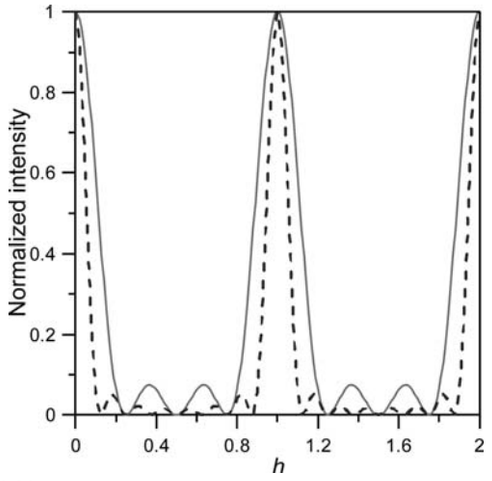

Figure 1.1.20
Normalized intensity from a finite lattice with $n = 3$ (solid curve) and $n = 8$ (dashed line), demonstrating the sharpening of peaks with increasing number of unit cells n. The normalization was done such that the peaks have the same peak maximum rather than the same integrated intensity for a clearer comparison of the relative peak widths.

vation of the Scherrer equation following Klug & Alexander (1974).

Fig. 1.1.21 shows the path-length difference *versus* the depth of the lattice plane. When the angle between the incoming beam and the lattice plane θ is different by an amount ε from the Bragg condition, it is always possible to find a lattice plane inside an infinite crystal where the extra path is $\Delta = \lambda(n + \frac{1}{2})$ for n integer, producing destructive interference. For a thick crystal this is true for arbitrarily small ε, which explains the sharp Bragg reflections. In the case of a crystal with finite dimensions, for small ε the plane for which $\Delta = \lambda(n + \frac{1}{2})$ holds will not be reached, thus leading to an intensity distribution over some small angular range. We can use this idea to estimate the broadening of a Bragg reflection due to size effects.

The thickness of a crystallite in the direction perpendicular to p planes of separation d_{hkl} (Fig. 1.1.21) is

$$L_{hkl} = pd_{hkl}. \tag{1.1.68}$$

The additional beam path between consecutive lattice planes at the angle $\theta + \varepsilon$ is

$$\begin{aligned}\Delta &= 2d\sin(\theta + \varepsilon)\\ &= 2d(\sin\theta\cos\varepsilon + \cos\theta\sin\varepsilon)\\ &= n\lambda\cos\varepsilon + 2d\sin\varepsilon\cos\theta\\ &\simeq n\lambda + 2d\sin\varepsilon\cos\theta.\end{aligned} \tag{1.1.69}$$

The corresponding phase difference is then

$$\delta\varphi = 2\pi\frac{\Delta}{\lambda} = 2\pi n + \frac{4\pi}{\lambda}\varepsilon d\cos\theta = \frac{4\pi\varepsilon d\cos\theta}{\lambda} \tag{1.1.70}$$

and the phase difference between the top and the bottom layer (layer p) is then

$$p\delta\varphi = p\frac{4\pi\varepsilon d\cos\theta}{\lambda} = \frac{4\pi L_{hkl}\varepsilon\cos\theta}{\lambda}. \tag{1.1.71}$$

Rearranging equation (1.1.71) leads to

$$\varepsilon = \frac{\lambda\delta\varphi}{4\pi L_{hkl}\cos\theta}, \tag{1.1.72}$$

which gives an expression for the misalignment angle in terms of the crystallite size L_{hkl} and the phase difference $\delta\varphi$ between the reflections originating from the top plane and the bottom plane. Clearly, the scattered intensity is at a maximum for $\delta\varphi = 0$ ($\varepsilon = 0$). With increasing ε the intensity decreases, giving rise to a peak of finite width. Perfect cancellation of the waves from the top and bottom planes occurs for a phase difference of $\delta\varphi = \pm\pi$, at which point $\varepsilon = \pm\lambda/(4L_{hkl}\cos\theta)$. On a 2θ scale, the measured angular width between these points is

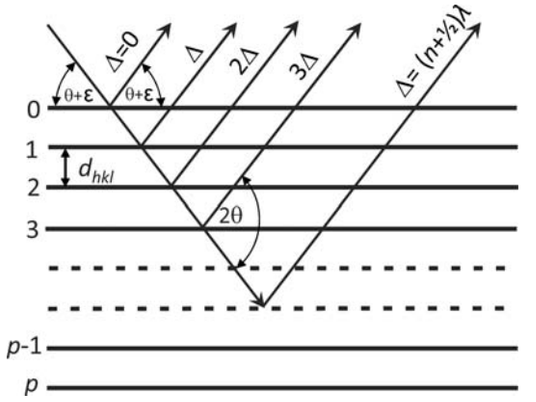

Figure 1.1.21
Path-length difference of the scattered ray *versus* the depth of the lattice plane in the crystal. [Reproduced from Dinnebier & Billinge (2008) with permission from the Royal Society of Chemistry.]

$$\beta_{hkl} = 4\varepsilon = \frac{\lambda}{L_{hkl}\cos\theta}, \tag{1.1.73}$$

giving us some measure of the peak width in radians that results from the finite particle size. A full treatment taking into account the correct form for the intensity distribution gives

$$\beta_{hkl} = \frac{K\lambda}{L_{hkl}\cos\theta}, \tag{1.1.74}$$

with a scale factor of $K = 0.89$ for perfect spheres. In general K depends on the shape of the grains (*e.g.* K is 0.94 for cube-shaped grains), but it is always close to unity. This equation is not valid for crystallites[3] that are too large or too small. In the case of large crystallites the peak width is governed by the coherence of the incident beam and not by particle size. For nanometre-sized crystallites, Bragg's law fails and the Debye equation needs to be used instead. The Debye equation (see Section 1.1.5.3) gives the scattering from an isotropically scattering sample such as a glass, liquid or powder, and does not presume that the sample is periodic.

1.1.4.1.2. *Microstrain*

Several important relationships in crystallography, including the effect of strain and microstrain on Bragg peaks, follow directly from a derivative of the Bragg equation (1.1.3). First we rewrite Bragg's law making the d-spacing the subject of the equation:

$$d = \frac{n\lambda}{2\sin\theta}. \tag{1.1.75}$$

The uncertainty of the measured lattice spacing is given by the total derivative dd,

$$\mathrm{d}d = \frac{\partial d}{\partial\theta}\mathrm{d}\theta + \frac{\partial d}{\partial\lambda}\mathrm{d}\lambda, \tag{1.1.76}$$

[3] Strictly speaking, the term crystallite size here refers to the dimension of a coherently scattering domain. Only in a perfect crystal is this the grain size.

Table 1.1.1
Types of scattering from a sample

Type of scattering	Coherent	Incoherent
Elastic	Bragg scattering Magnetic Bragg scattering Bragg scattering from ferroelectric/magnetic order Diffuse scattering from static defects Diffuse signal from small nanoparticles (<10 nm) Scattering from amorphous material (except excitations) Multiple scattering (coherent)	Laue monotonic diffuse scattering Neutron incoherent scattering Multiple scattering (incoherent)
Inelastic	Thermal diffuse scattering Spin-wave scattering Paraelectric/paramagnetic scattering Scattering from liquids	Compton scattering Fluorescence Incoherent scattering from hydrogen

leading to

$$\mathrm{d}d = -\frac{n\lambda}{2\sin\theta}\frac{\cos\theta}{\sin\theta}\mathrm{d}\theta + \frac{n}{2\sin\theta}\mathrm{d}\lambda \qquad (1.1.77)$$

and finally

$$\frac{\mathrm{d}d}{d} = -\frac{\mathrm{d}\theta}{\tan\theta} + \frac{\mathrm{d}\lambda}{\lambda}. \qquad (1.1.78)$$

When a crystal is strained, the d-spacings vary. A *macroscopic* strain changes the interplanar spacing by Δd_{hkl}, giving rise to a shift of $\Delta\theta$ in the *average* position of the diffraction peak. On the other hand, *microscopic* strains result in a distribution of d-spacings of width δd_{hkl}, which has the effect of *broadening* the diffraction peak by $\delta\theta$. Equation (1.1.78) gives an expression for the amount of Bragg-peak broadening that occurs for a given δd_{hkl}.

1.1.5. The background

1.1.5.1. *Information content in the background*

As discussed above, the elastic scattering from a crystalline powder consists of sharp rings, or peaks, of scattering at the 2θ angles where the Bragg or von Laue laws are satisfied. In general these sharp peaks sit on top of a 'background' which is broad and somewhat featureless. There are two components to this background, illustrated in Fig. 1.1.1: extraneous counts in the detector from things other than the sample, and non-Bragg scattering from the sample itself. The former are rarely of interest scientifically and the objective of a good experimental design is to minimize them as far as possible, or explicitly measure and subtract them, and then account well in any model or data interpretation for the part that cannot be eliminated from the measurement. Historically, the diffuse-scattering signals from the sample itself were also considered to be an inconvenience to be minimized and removed, and indeed in many cases this is still the best course of action (for example, sample fluorescence can be eliminated by choosing to work at an X-ray energy that lies below the absorption edge of a constituent atom). However, the diffuse 'background' from the sample can contain crucial information about defects, disorder and nanoscale order in the sample, and increasingly we are interested in studying it in order to understand the properties of the material that is under investigation. In some cases, such as glasses, liquids and samples of small nanoparticles, there is no Bragg scattering at all and only a diffuse scattering signal (see Chapter 5.6).

All the intensity scattered by the sample can be categorized as either coherent or incoherent and as elastic or inelastic, which are defined as follows. The coherency of the signal derives from whether or not the scattered waves interfere with each other constructively, and the resulting intensities are different in each case. For coherent scattering, the waves contributing to the signal are all summed first, before the wave amplitude is squared, to find the intensity distribution, which is the modulus squared of the resulting wave. For incoherent waves, one simply squares the amplitude of each wave to get its intensity and sums these together to get the total intensity. Switching to a consideration of the elasticity of the scattering, we define the scattering as elastic if the incident and scattered waves have the same energy, in which case no energy was exchanged during the scattering process between the incident wave and the sample, and inelastic scattering as the opposite. Inelastic scattering may result in a gain or a loss of energy of the scattered particle depending on the nature of the scattering, which results in a change in the wavelength of the scattered particle. There are also some non-scattering processes that can take place, such as absorption and fluorescence, but emissions resulting from these processes can also be categorized by whether or not they are coherent and elastic. It should be noted that the total energy of the system must be conserved during the scattering process, and so when a scattered wave gains or loses energy it exchanges it with the sample. This is used as a way of probing excitations in a material. Table 1.1.1 summarizes many of the types of diffuse scattering coming from a sample and categorizes them by their coherency and elasticity.

1.1.5.2. *Background from extraneous sources*

The most commonly observed extraneous, or parasitic, scattering is from the sample container (such as a capillary) that holds the sample during the measurement. Another large contribution may come from air scattering, which originates principally from scattering of the direct beam by molecules in the air in the beam path, both before and after the sample. Air-scattering effects can be minimized by enclosing as much of the beam path as possible in a tube which may be evacuated or where the air is replaced by a weakly scattering gas (such as He in the case of X-rays). Air scattering that is detected by the detector can also be reduced by careful collimation of the beams and then shielding the detector from detecting radiation that does not originate from the sample position. Collimating the incident beam is straightforward and results in a big reduction in air scattering. For point detectors it is also straightforward to collimate the scattered beam, but the modern trend towards using linear and area detectors makes this more difficult. There is sometimes a trade-off between collimating the scattered beam to reduce background and having uniform backgrounds that do not vary with angle because of

incomplete angle-dependent collimation. Incomplete angle-dependent collimation can be very difficult to correct when trying to measure diffuse scattering quantitatively and the current trend is to have minimal secondary collimation.

There is increasing interest in carrying out *in situ* experiments under extreme conditions of pressure, temperature, magnetic field and so on (see Chapters 2.6 to 2.8). These experiments inevitably introduce additional scattering from the environment. Again, there is a balance between finding creative ways to reduce these backgrounds, and simply making them less problematic in the data analysis. For example, in a diamond-anvil cell, where the beam accesses the sample through the diamond, one can drill a hole part way through the diamond to accommodate the direct beam and make the direct beam small enough to fit in the hole. This increases the complexity of the measurement as alignment becomes harder, but it is usually worth it. Shielding structural parts of the environment cell with an absorbing material, such as lead for X-rays or a borated material for neutrons, can help to reduce unwanted background intensity a lot, as can making thin, transparent windows for the incident and scattered beams.

An additional source of background in the signal does not come from scattering at all, but from electrical noise in the detector electronics. For some types of detectors it may be important to measure 'dark' exposures with the X-rays turned off and subtract these carefully from the experimental data. It is also possible to detect signals from cosmic rays, which can leave tracks in two-dimensional detector signals.

1.1.5.3. *Sources of background from the sample*

1.1.5.3.1. *Elastic coherent diffuse scattering*

As discussed in Section 1.1.4.1.1, decreasing the size of a crystal leads to an increase in the width of the Bragg peaks. When the size of the crystallite becomes very small, as a rule of thumb below 10 nm in diameter for typical unit cells, the widths of the Bragg peaks become so large that they merge and overlap, and it does not make sense to use delta-function Bragg peaks as the starting point for the analysis. At this point the coherent diffraction is completely diffuse in nature. Nonetheless, it still contains structural information. To see this we begin again with the Laue equation before we assumed periodicity [equation (1.1.39)]. For the simple case of a diatomic gas such as N_2, the sum would be taken only over two atoms, since scattering from a single molecule will be coherent but that from different molecules will be incoherent. In that case we have

$$A(\mathbf{h}) = \sum_{j=1}^{2} f_j(h)\exp(2\pi i\mathbf{h}\cdot\mathbf{r}_j),$$
$$A(\mathbf{h}) = f_1\exp(2\pi i\mathbf{h}\cdot\mathbf{r}_1) + f_2\exp(2\pi i\mathbf{h}\cdot\mathbf{r}_2), \tag{1.1.79}$$

and the intensity is proportional to

$$I(\mathbf{h}) = (f_1f_1^* + f_2f_2^*) + f_1f_2^*\exp\left(2\pi i\mathbf{h}\cdot\mathbf{r}_{12}\right) + f_2f_1^*\exp\left(-2\pi i\mathbf{h}\cdot\mathbf{r}_{12}\right), \tag{1.1.80}$$

where $\mathbf{r}_{12} = \mathbf{r}_1 - \mathbf{r}_2$. For a diatomic molecule where both atoms are the same $f_1 = f_2$ and

$$I(\mathbf{h}) = f^*f\cos^2(\pi\mathbf{h}\cdot\mathbf{r}_{12}). \tag{1.1.81}$$

The scattering from a diatomic molecule of an element is simply a single-component cosine wave with a wavelength that depends on the separation of the atoms in the molecule. In an actual experiment there will be scattering from all the molecules that have every orientation with equal probability, so it is necessary to take an orientational average of the scattering. How this is done is shown in Chapter 5.7 on PDF analysis, but the result is the Debye equation (Debye, 1915),

$$I(h) = \frac{1}{N\langle f\rangle^2}\sum_{i,j} f_j^*f_i\left[\frac{\sin(Qr_{ij})}{Qr_{ij}}\right], \tag{1.1.82}$$

where N is the total number of atoms. For our diatomic molecule this becomes

$$I(h) = \frac{1}{N}\left[\frac{\sin(Qr_{ij})}{Qr_{ij}}\right]. \tag{1.1.83}$$

For clusters of atoms such as larger molecules or small nanoparticles that are intermediate in size between a diatomic molecule and a small chunk of crystal, the Debye equation is exact and may be used to calculate the intensity of the scattering. As the clusters get larger and the structure more periodic, such as small chunks of crystal, the scattering calculated from the Debye equation crosses smoothly to that obtained from the periodic Laue equation. The finite size broadened crystallographic model works well as a starting point for calculating scattering from well ordered crystals down to nanoparticle sizes of 10 nm, but loses accuracy rapidly below this particle size. The Debye equation is accurate for all particle sizes, but becomes computationally intractable for larger clusters much above 10 nm.

1.1.5.3.2. *Total-scattering and atomic pair distribution function analysis*

An alternative approach to the analysis of diffuse scattering from nanostructures is to Fourier transform the data to obtain the atomic pair distribution function, or PDF. In fact, the Fourier transform does not depend on whether the structure is periodic or not, and it is also possible to Fourier transform the Bragg scattering from crystals. If there is no nanoscale disorder in the crystal there are few real benefits in doing this rather than using the powerful crystallographic methods described elsewhere in this chapter. However, the PDF approach utilizes both the Bragg *and* diffuse components, and yields additional information about the structure that is particularly valuable when the crystal contains some kind of nanoscale domains. The presence of such domains was rarely considered in the past, but we now know that they are often found in materials. In the sense that both Bragg and diffuse scattering data are used without prejudice, and also that the data are measured over a wide range of the scattering vector so that, as far as possible, the coherent scattering in all of the reciprocal space is measured, this method is known as 'total-scattering analysis', and as 'PDF analysis' when the data are Fourier transformed and studied in real space.

The powder diffraction data for total-scattering studies are measured in much the same way as in a regular powder diffraction experiment. However, explicit corrections are made for extrinsic contributions to the background intensity from such effects as Compton scattering, fluorescence, scattering from the sample holder and so on. The resulting coherent scattering function $I(Q)$ is a continuous function of $Q = |\mathbf{Q}| = 2h = 4\pi\sin\theta/\lambda$, with sharp peaks where there are Bragg reflections and broad features in between. In general it is usual to work with a normalized version of this scattering intensity, $S(Q)$. This is the intensity normalized by the incident flux per atom in the sample. $S(Q)$ is called the total-scattering structure function. It is a dimensionless quantity and the normalization is such that the average value $\langle S(Q)\rangle = 1$. In short, $S(Q)$ is nothing other than the powder diffraction pattern that

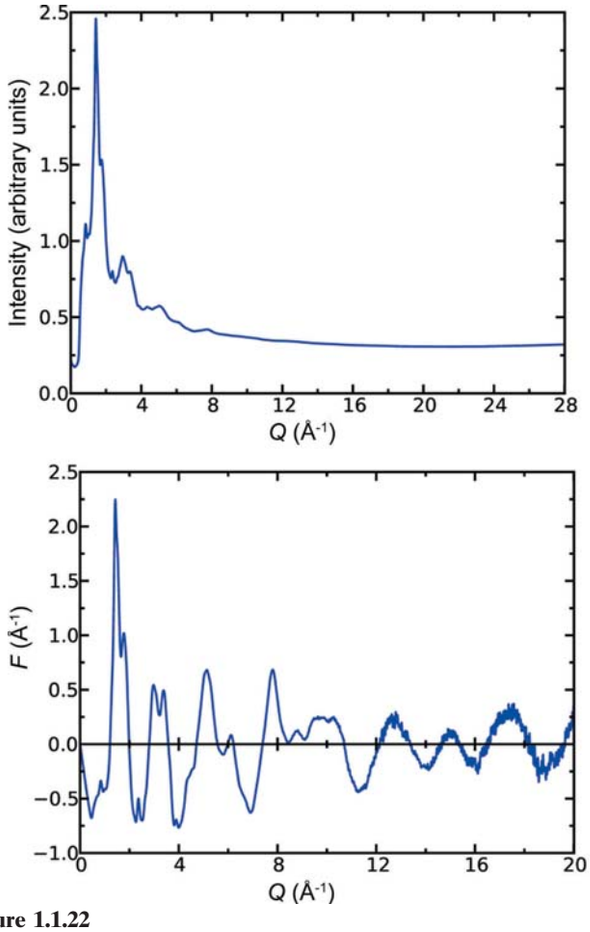

Figure 1.1.22
Comparison of raw data and the normalized reduced total-scattering structure function $F(Q) = Q[S(Q) - 1]$. The sample is a powder of 2 nm diameter CdSe nanoparticles and the data are X-ray data from beamline 6ID-D at the Advanced Photon Source at Argonne National Laboratory. The raw data are shown in the top panel. The high-Q data in the region $Q > 9$ Å^{-1} appear smooth and featureless. However, after normalizing and dividing by the square of the atomic form factor, important diffuse scattering is evident in this region of the diffraction pattern (bottom panel).

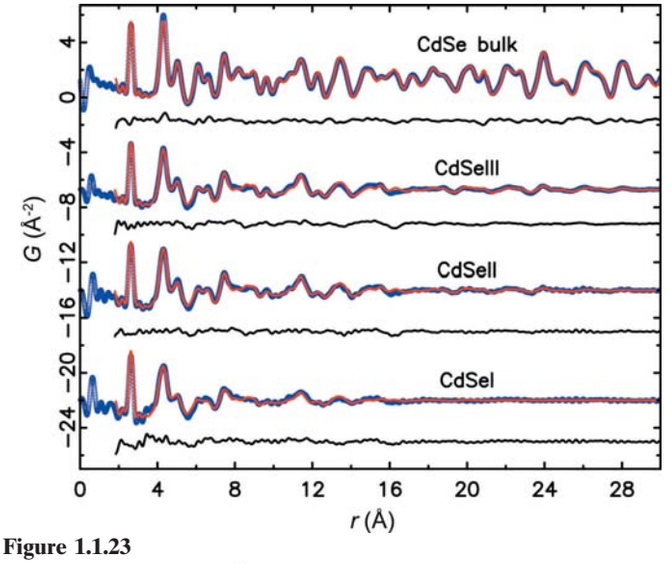

Figure 1.1.23
PDFs in the form of $G(r)$ from bulk CdSe and from a series of CdSe nanoparticles. The blue curve at the bottom is the PDF obtained from the data shown in Figure 1.1.22. The blue symbols are from the data and the thin red lines on top are from models of the local structure in these nanoparticles. Offset below are difference curves between the model and the data. [Reprinted with permission from Masadeh *et al.* (2007). Copyright (2007) by the American Physical Society.]

has been corrected for experimental artifacts and suitably normalized (Egami & Billinge, 2013).

Measuring over a wide range of Q values yields better resolution in real space, as well as yielding more information, and is desirable. The coherent intensity (the features) in $S(Q)$ dies out with increasing Q because of the Debye–Waller factor (which comes from thermal and quantum zero-point motion of the atoms), as well as any static displacive disorder in the material and, for X-ray measuerments, because of the X-ray form factor. In a neutron measurement, the atomic displacement effects are still present, but the neutron has no form factor and the scattering length is constant in Q. By a Q value of 30–50 Å^{-1} (depending on the temperature and the stiffness of the bonding in the sample) there are no more features in $S(Q)$ and there is no need to measure data to higher Q. Still, this is a much higher maximum value of Q than is measured in conventional powder diffraction experiments using laboratory X-rays or reactor neutrons. The maximum value of Q attainable in back scattering from a Cu $K\alpha$ tube is around 8 Å^{-1} and from an Mo $K\alpha$ tube it is around 16 Å^{-1}. Routine total-scattering measurements can be made using laboratory sources with Mo or Ag tubes; however, for the highest real-space resolution, and the smallest statistical uncertainties, synchrotron data are preferred. In the case of neutron scattering, spallation neutron sources are ideal for total-scattering experiments.

The total-scattering function $S(Q)$ appears to be different from the function measured in a standard powder diffraction experiment because of the Q range studied, and also because of an important aspect of the normalization: the measured intensity is divided by the total scattering cross section of the sample. In the case of X-ray scattering, the sample scattering cross section is the square of the atomic form factor, $\langle f(Q)\rangle^2$, which becomes very small at high Q. Thus, during the normalization process the data at high Q are amplified (by being divided by a small number), which has the effect that even rather weak intensities at high Q, which are totally neglected in a conventional analysis of the data, become rather important in a total-scattering experiment. Because the signal at high Q is weak it is important to collect the data in that region with good statistics. This is illustrated in Fig. 1.1.22.

The Fourier transform of the total-scattering data is the reduced pair distribution function, $G(r)$, which is related to $S(Q)$ through a sine Fourier transform according to

$$G(r) = \frac{2}{\pi}\int_{Q_{\min}}^{Q_{\max}} Q[S(Q) - 1]\sin(Qr)\,\mathrm{d}Q. \qquad (1.1.84)$$

Examples of $G(r)$ functions from small nanoparticles of CdSe are shown in Fig. 1.1.23.

$G(r)$ has peaks at positions, r, that separate pairs of atoms in the solid with high probability. For example, there are no physically meaningful peaks below the nearest-neighbour peak at ~2.5 Å, which is the Cd–Se separation in CdSe. However, in addition to the nearest-neighbour information, valuable structural information is contained in the pair correlations that extend to much higher values of r. In fact, with data to a high resolution in Q, PDFs can be measured out to hundreds of nanometres (*i.e.*, thousands of ångströms) and the structural information that can be obtained from the data remains quantitatively reliable (Levashov *et al.*, 2005).

The function $G(r)$ is related to the atomic density. However, it is not the atomic density itself, but its autocorrelation. This is

obtained by taking the atomic density of the molecule or cluster (which are the atoms at their respective positions) and convoluting it with a replica of the same thing. This object is then orientationally averaged to obtain the PDF. It is not a particularly intuitive object, but it is straightforward to calculate it from a given structural model. The inverse problem, calculating the structure from a PDF, is not possible directly, although in favourable cases, as with structure solution from powder diffraction, it is possible to obtain a unique structure solution from a PDF (Juhás *et al.*, 2006).

We described above how to obtain $G(r)$ from powder data. Here we briefly describe how to calculate a PDF from a structural model. To do this we have to introduce a related function to the PDF, the radial distribution function (RDF), $R(r)$, which is related to $G(r)$ by

$$G(r) = \frac{R(r)}{r} - 4\pi r\rho_0, \tag{1.1.85}$$

where ρ_0 is the atomic number density (Egami & Billinge, 2013).

The function $R(r)$ is important because it is more closely related to the physical structure than $G(r)$, since $R(r)\,\mathrm{d}r$ gives the number of atoms in an annulus of thickness $\mathrm{d}r$ at distance r from another atom. For example, the coordination number (or the number of neighbours) of an atom, N_C, is given by

$$N_\mathrm{C} = \int_{r_1}^{r_2} R(r)\,\mathrm{d}r, \tag{1.1.86}$$

where r_1 and r_2 define the start and end positions of the RDF peak corresponding to the coordination shell in question. This suggests a scheme for calculating PDFs from atomic models. Consider a model consisting of a large number of atoms situated at positions $\mathbf{r}_\nu$ with respect to some origin. Expressed mathematically, this amounts to a series of delta functions, $\delta(\mathbf{r} - \mathbf{r}_\nu)$. The RDF is then given as

$$R(r) = \frac{1}{N}\sum_\nu \sum_\mu \delta(r - r_{\nu\mu}), \tag{1.1.87}$$

where $r_{\nu\mu} = |\mathbf{r}_\nu - \mathbf{r}_\mu|$ is the magnitude of the separation of the νth and μth ions, and the double sum runs twice over all atoms in the sample. In Chapter 5.7 on PDF analysis we address explicitly samples with more than one type of atom, but for completeness we give here the expression for $R(r)$ in this case:

$$R(r) = \frac{1}{N}\sum_\nu \sum_\mu \frac{f_\nu f_\mu}{\langle f\rangle^2}\delta(r - r_{\nu\mu}), \tag{1.1.88}$$

where f_ν and f_μ are the form factors, evaluated at $Q = h = 0$, for the νth and μth atoms, respectively, and $\langle f\rangle$ is the sample-average form factor.

1.1.5.3.3. *Inelastic coherent diffuse scattering*

Scattering events must conserve energy and momentum. When a wave is scattered it changes direction and therefore changes its momentum. To satisfy conservation, this momentum, $\mathbf{Q} = 2\pi\mathbf{h} = 2\pi(\mathbf{s} - \mathbf{s}_0)$, must be transferred to the material. When radiation is scattered by a crystal, the mass of the crystal is so large that this produces a negligible acceleration and the scattering is elastic. However, scattering from free atoms or fluids will produce a recoil, which results from a transfer of energy to the atom and the scattering is strictly inelastic. Even within a bulk crystal, there are lattice excitation modes (phonons) which may be created during a particular scattering event and the resulting scattering is inelastic. In an X-ray experiment, the energy resolution of the measurement usually is much too poor to separate this from the elastic scattering and it all appears mixed together (and is often simply referred to as 'elastic scattering'). As the excitation energies of internal modes of the system have energies of the order of meV (10^{-3} eV) and the X-ray energy is of the order of keV (10^3 eV), resolving the inelastic modes would require an energy resolution of $\Delta E/E = 10^{-6}$, which is often unachievable. Nonetheless, such experiments are now carried out at synchrotron sources and provide important scientific insights, although the experiments are very slow and very specialized (Burkel, 1991).

These experiments are rarely carried out on powders. If the inelastic scattering is not resolved during the measurement, as is usually the case, it appears as a diffuse-scattering component in the signal from the powder or single crystal and it can be interpreted and modelled to extract information. In powder diffraction, when the scattering occurs from lattice vibrations, or phonons, the diffuse signal is called 'thermal diffuse scattering' or TDS (Warren, 1990). Over the last 50–60 years, a number of attempts have been made to extract information about phonon energies and phonon dispersions from TDS with varying amounts of success (Warren, 1990; Jeong *et al.*, 1999; Graf *et al.*, 2003; Goodwin *et al.*, 2005). In the case of PDF analysis, the information in the TDS manifests itself in real space as correlated motion, and it is observed that the low-r peaks are sharper than the high-r peaks. This is because closely bonded atoms tend to move together: if an atom moves to the right it tends to push its neighbour also over to the right, so the motion is correlated. There is useful information in the TDS and the r dependence of the PDF peak broadening, but this is at best a very indirect way of measuring lattice-dynamical effects.

When the energy transfer is not resolved it is hard to separate the cases of scattering arising from phonons (which are dynamic atomic displacements) and scattering arising from static atomic displacements. To some extent these can be disentangled by studying the temperature dependence of the atomic displacement parameters (ADPs) obtained from modelling the data either in reciprocal space or real space (Billinge *et al.*, 1991). This is often done by using a Debye model (Debye, 1912), where the temperature dependence of the mean-square ADP is given by

$$\overline{u^2} = \left(\frac{3h^2T}{4\pi^2 M k_B \theta_D^2}\right)\left[\varphi\left(\frac{\theta_D}{T}\right) + \frac{1}{4}\frac{\theta_D}{T}\right] + A_\mathrm{offset}, \tag{1.1.89}$$

where

$$\varphi\left(\frac{\theta_D}{T}\right) = \frac{T}{\theta_D}\int_0^{\theta_D/T}\left[\frac{x}{\exp(x) - 1}\right]\mathrm{d}x, \tag{1.1.90}$$

is the Debye integral. Here, θ_D is the Debye temperature, which is a measure of the stiffness of the bonding, h and k_B are Planck's and Boltzmann's constants, respectively, and M is the mass of the oscillating atom. The constant A_offset is a temperature-independent offset that is generally needed in the model to account for static distortions. The Debye model is rather crude but surprisingly useful and works well in many cases.

As in the case of phonons, if the scatterer couples to something else in the solid that has an excitation spectrum, this can be studied too. The case of neutrons scattered by magnetic moments is the best known example. Inelastic scattering gives direct information about the magnon dispersion curves. Information about magnetic excitations may also be obtained indirectly from

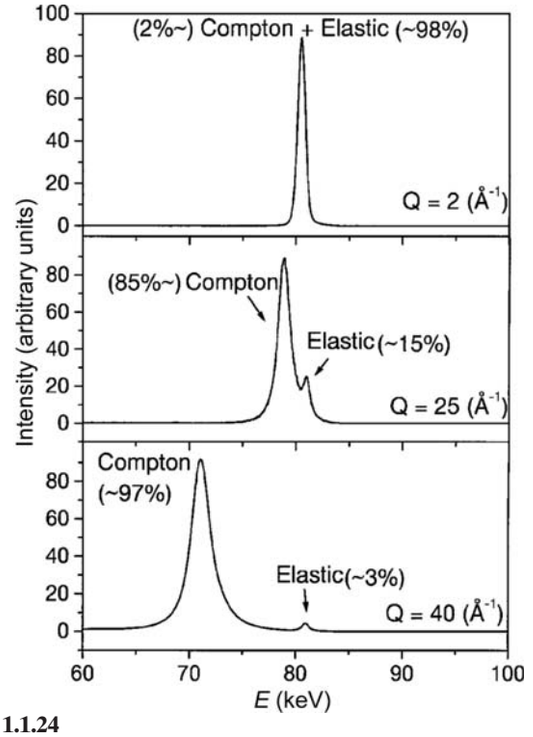

Figure 1.1.24
Spectrum from an energy-resolving detector that shows the elastic and Compton signals as a function of scattering vector **Q**. [Reprinted with permission from Petkov *et al.* (2000). Copyright (2007) by the American Physical Society.]

the non-energy-resolved magnetic diffuse scattering signal. Magnetic PDF is now possible (Frandsen & Billinge, 2015) as described in Chapter 5.7, as well as reciprocal-space studies of magnetic diffuse scattering (Paddison & Goodwin, 2012).

1.1.5.3.4. *Incoherent scattering*

Incoherent scattering does not contain any structural information, and cannot be used to study structure in a diffraction experiment since the intensities of the scattered waves do not depend on the position of the scatterers. This does not mean that all incoherent scattering intensity is useless. The fluorescence intensity is incoherent, but may be used in EXAFS experiments to yield structural information. This is because coherent scattering of the photoexcited electron during an absorption event modulates the absorption cross section and therefore the incoherent fluorescence intensity, so a coherent scattering process leaves a measurable response in an incoherent intensity. Incoherent scattering can also be used to measure excitations, although all momentum-transfer information is lost so it is not possible to measure, for example, dispersions of excitations such as phonons and magnons. Even if the scattering process is incoherent, the energy exchanged between the probe and the sample can be measured by the change in wavelength of the scattered wave, and the amplitude of the scattering at each energy transfer is proportional to the density of states of the excitation being probed. In the case of neutrons, the very large incoherent cross section for scattering by hydrogen ($\sim$100$\times$ the scattering cross section of most atoms) provides a strong signal for studying low-probability inelastic scattering events. Measuring inelastic scattering from powders can be a rapid way of determining the density of states of phonons, magnons and so on, which is very useful for determining the thermodynamic properties of materials, even though it is less precise than measurement of the full set of dispersion curves.

Another type of incoherent scattering that can be observed in X-ray experiments is Compton scattering (Compton, 1923; Cooper *et al.*, 2004), which is an inelastic incoherent process where the scattering atom recoils during the scattering event. An example of Compton scattering measured in the spectrum from an energy-resolving detector is shown in Fig. 1.1.24.

The Compton scattering is strong in this experiment because the incident X-ray energy is high (80 keV) and the sample is a low-atomic-number alumina-silicate glass. Both the high X-ray energy and the low atomic numbers of the atoms in the sample increase the Compton cross section with respect to the coherent elastic scattering. As the magnitude of the scattering vector, Q, is increased the Compton scattering moves to lower energy and increases in intensity, but the elastic line stays fixed in energy and its intensity decreases because of form-factor and Debye–Waller effects. Momentum as well as energy is conserved in this process and the Compton scattering can be used to measure the momentum distribution of electrons in a material, although this kind of experiment is not widespread these days.

Elastic incoherent scattering provides no information about the sample, and simply degrades the signal-to-noise ratio of the measurement. As such, it is just inconvenient and cannot be easily removed. Monotonic Laue diffuse scattering originates from different chemical species with different scattering powers residing on different sites in the crystal, and when a destructive interference condition is satisfied the resulting intensity does not go to zero but is proportional to $[f_i(h) - f_j(h)]^2$ (Warren, 1990). In pure elements in an X-ray experiment, the atoms on every site are the same and there is no Laue diffuse scattering. This is not true in neutron experiments where different nuclei have different scattering powers and most elements contain a range of isotopes in their natural form (the 'natural abundance'; Squires, 1996). This results in Laue diffuse scattering even in an element, although it is normally not referred to in these terms but is encompassed by a so-called 'incoherent neutron cross section' that is defined and tabulated (see Table 4.4.4.1 in *International Tables for Crystallography*, Volume C) for each element. This is not the only source of incoherent scattering in neutron diffraction, since the scattering power also depends on the relative orientation of the neutron and nuclear spins. In general these spins are all orientationally disordered (and fluctuating) and the result is an additional scattering-event-dependent contribution to the incoherent scattering from the sample, again encompassed by the 'incoherent neutron cross section' of the element. Where necessary, it may be possible to make isotopically enriched samples for neutron experiments so that the proportion of isotopes with large incoherent scattering cross sections is minimized (or the isotopes are removed altogether), and the range of isotopes can also be reduced, which further reduces the incoherent component of the signal. However, the cost and difficulty of doing this means that it is rarely done.

1.1.6. Local and global optimization of crystal structures from powder diffraction data

1.1.6.1. *Rietveld refinement*

More than 40 years have passed since the publication of the pioneering papers by Hugo Rietveld (Rietveld, 1967, 1969), in which he described a method for the refinement of crystal structures from neutron powder diffraction data. Neutron data sets from reactor sources were more amenable than X-ray data sets to this method because the line profiles are quite Gaussian.

However, it was not long before the method was extended to X-ray powder diffraction. The quality of the data and the computation power available these days have allowed the technique to develop enormously, to the point that even the (successful) Rietveld refinement of small protein structures from synchrotron powder diffraction data is now possible (see Chapter 7.1). Another development is the extension of the Rietveld method towards parametric refinement on large numbers of complimentary data sets with various as-yet unexplored new applications. Rietveld refinement is so important it is described in detail in Chapter 4.7, but we describe a number of important fundamentals of the method here by way of introduction.

The basic idea behind the Rietveld method is simple: Instead of extracting the integrated intensities of Bragg peaks and fitting models to these, as would be done in single-crystal and early powder diffraction studies, the full powder pattern, for example available as step-scanned intensity data, is fitted using a model whose parameters are refined using a least-squares procedure. The model parameters are varied in such a way as to minimize the sum of the squares of the difference between the n observed $Y\mathrm{obs}_i$ and n calculated $Y\mathrm{calc}_i(\{p\})$ step-scan intensities in the powder pattern, where the latter are calculated from a model containing a set of parameters $\{p\}$. The function that is minimized is usually the profile-weighted residual function, or R factor, given by

$$R_w = \sum_{i=1}^{n} w_i \big(Y\mathrm{obs}_i(2\theta) - Y\mathrm{calc}_i(2\theta; \{p\})\big)^2. \qquad (1.1.91)$$

The weight w_i is derived from the variance of the values of $Y\mathrm{obs}_i$, while all covariances between different $Y\mathrm{obs}_i$ values are assumed to be zero.

The calculated intensity $Y\mathrm{calc}_i$ is expressed by combinations of mostly nonlinear and analytic or non-analytic functions as

$$Y\mathrm{calc}_i = \sum_{ph=1}^{\text{phases}} \left(S_{ph} \sum_{hkl(ph)} \left(K_{hkl(ph)} \left|F_{hkl(ph)}\right|^2 \Phi_{hkl(ph)}\left(2\theta_i - 2\theta_{hkl(ph)}\right)\right)\right) + b_i(\mathrm{obs}). \qquad (1.1.92)$$

The outer sum runs over all phases ph present in the powder pattern, while the inner sum runs over all reflections hkl of a phase ph that contribute to the intensity at the position i in the powder pattern. A scaling factor S_{ph} is assigned to the reflection intensities for each phase; the scaling factor is proportional to the weight fraction of the phase. $K_{hkl(ph)}$ represents the product of various correction factors to the square of the structure-factor amplitudes, $\left|F_{hkl(ph)}\right|^2$, which may depend on the diffraction geometry and/or individual reflections. The value of the profile function $\Phi_{hkl}(2\theta_i - 2\theta_{hkl})$ is given for the profile point $(2\theta_i - 2\theta_{hkl})$ relative to the position of the Bragg reflection hkl. The observed background at position i in the powder pattern is denoted as $b_i(\mathrm{obs})$. Parameters in the model such as atomic positions, lattice parameters and experimental factors that affect peak shape and background are varied, using a least-squares approach, until the agreement between the calculated and measured diffraction profiles is optimized. In a least-squares approach, optimization consists of minimizing a cost function that is the weighted sum of the squared differences. This is a refinement method: a good initial guess at, or knowledge of, the structure is required and this model is refined by small adjustments.

This approach requires the modelling of the *entire* powder pattern. To simplify this complex task, the information content of the powder pattern can be divided into several parts (Fig. 1.1.1), allowing the separation of groups of parameters with respect to their origin:

(*a*) the peak intensity $\left|F_{hkl(ph)}\right|^2$ – the time- and space-averaged crystal structure and geometrical contributions;
(*b*) the peak position – crystallographic lattice and symmetry, and instrumental contributions;
(*c*) the peak shape $\Phi_{hkl}(2\theta_i - 2\theta_{hkl})$ – microstructural parameters and instrument profile;
(*d*) the background $b_i(\mathrm{obs})$ – local structure and instrumental conditions.

Each part contains contributions from the sample and the instrument.

Rietveld refinement is a nonlinear least-squares process and requires starting values for all parameters. It is generally implemented with a local, rather than a global, optimizer and it is important for the starting parameters to be close to those of the actual solution to ensure that it is in the valley in parameter space that contains the global minimum. It is usual to guide the refinement into the (relatively narrow) range of convergence by hand by adding the parameters to the refinement sequentially. In this sense, Rietveld refinement takes some time to learn, but with care it can provide robust quantitative structures and a wealth of information can be extracted from the data.

Of course, there is no reason (other than computational efficiency) why the minimization algorithm could not be a more robust global optimizer, and this is now starting to be implemented in modern Rietveld codes. The most common and most easily implemented global optimizer, though one of the least efficient, is the Metropolis or simulated-annealing (SA) algo-

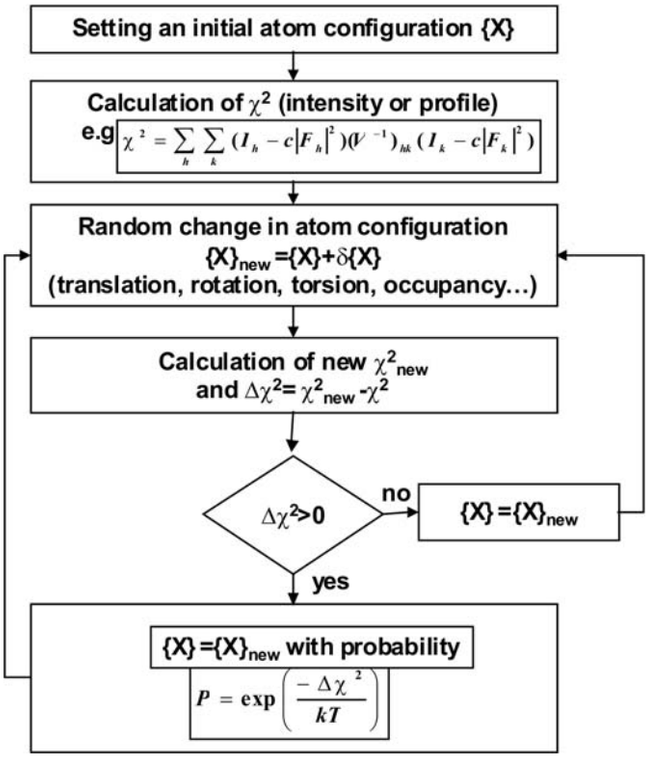

Figure 1.1.25
Flow diagram of a simulated-annealing procedure used for structure determination from powder diffraction data (from Mittemeijer & Welzel, 2012). F in the double sum is the structure factor from the structural model at each step of the optimization. Each sum runs over all reflections. h and k are summation indices representing hkl and $h'k'l'$, respectively.

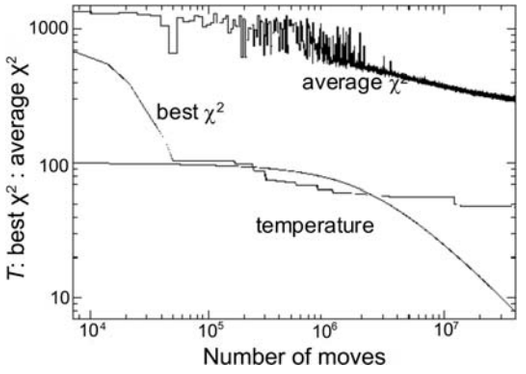

Figure 1.1.26
χ^2 (cost function) and 'temperature' dependence of the number of moves during a simulated-annealing run. [From Mittemeijer & Welzel (2012). Copyright Wiley-VCH Verlag GmbH & Co. KGaA. Reproduced with permission.]

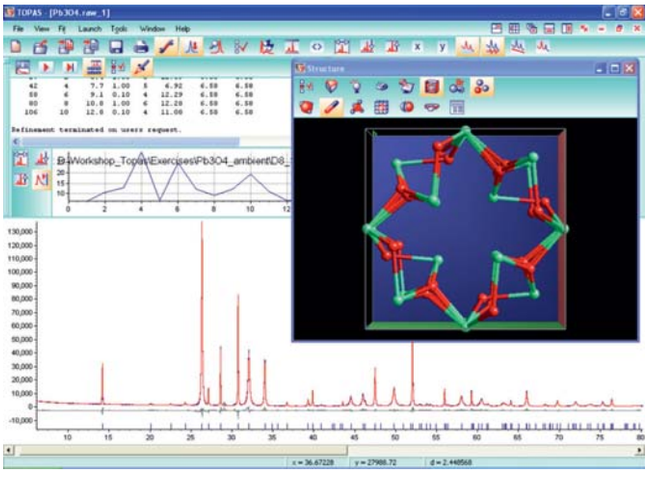

Figure 1.1.27
Screen shot (*TOPAS* 4.1; Bruker-AXS, 2007) of a simulated-annealing run on Pb_3O_4 measured with a D8 advance diffractometer in Bragg–Brentano geometry. [From Mittemeijer & Welzel (2012). Copyright Wiley-VCH Verlag GmbH & Co. KGaA. Reproduced with permission.]

rithm. The most usual implementation is actually as a 'regional' optimizer where the updates to parameters such as atomic position are constrained to be not too far from the previous values in such a way that the algorithm makes a random walk through the parameter space. This algorithm can avoid being trapped in a local minimum by 'walking uphill', since changes to the parameters that produce a worse agreement may be accepted with a probability based on the Boltzmann criterion, $\exp(-\Delta R/kT)$. The temperature in this expression is fictitious (*i.e.*, it does not refer to any real temperature) and ΔR is the change in the agreement produced by the trial update. The temperature plays the role of tuning the probability of accepting a bad move. It is initially chosen to have a high value, giving a high probability of escaping a minimum and allowing the algorithm to explore more of the parameter space. Later in the run the temperature is lowered, trapping the solution into successively finer valleys in the parameter space until it settles into (hopefully) the global minimum (Fig. 1.1.26). The calculation of R can be based on the entire profile, or on integrated intensities. For the latter, the correlation between partially or fully overlapping reflections must be taken into account (as shown schematically in Fig. 1.1.25).

A flow diagram of a typical SA algorithm as used for structure determination from powder diffraction data is shown in Fig. 1.1.25. Parameters that can be varied during the SA runs include internal and external degrees of freedom like translations (fractional coordinates or rigid-body locations), rotations (Cartesian angles, Eulerian angles or quaternions, describing the orientation of molecular entities), torsion angles, fractional occupancies, displacement parameters *etc*. Fig. 1.1.26 shows the results of a typical simulated-annealing run in which the cost function, χ^2, falls dramatically in the first few thousand moves, indicating that the scattering is dominated by the positioning of heavier atoms or globular molecules. Several million trial structures are usually generated before a minimum can be reached. At the end of the simulated-annealing run, Rietveld refinement is used to find the bottom of the global minimum valley.

Special algorithms are not usually used to prevent close contact of atoms or molecules during the global-optimization procedure, as in general these have not been found to be necessary, as the fit to the intensities alone quickly moves the molecules to regions of the unit cell where they do not grossly overlap with neighbouring molecules. A subsequent Rietveld refinement in which only the scale and overall displacement parameters are refined will immediately show whether further refinement of bond lengths and bond angles is necessary. Since unconstrained refinement often results in severe distortions from the ideal molecular geometry, either rigid bodies or soft constraints on bond lengths, the planarity of flat groups and bond angles can be used to stabilize the refinement. Another advantage of the simulated-annealing technique is that hydrogen atoms can often be included at calculated positions from the beginning if their relative position with respect to other atoms can be anticipated, which is often the case for molecular structures.

For inorganic crystal structures in particular, the identification of special positions or the merging of defined rigid bodies is useful during the final stages of structure solution. This can be accomplished by a so-called 'occupancy-merge' procedure as proposed by Favre-Nicolin & Černý (2004; see also Chapter 4.5). Here, the occupancies of the sites are modified as a function of the fractional coordinates, *i.e.* they are changed when the atoms get 'too close' to a special position. The sites are thought of as spheres with a radius r. In this way any number of sites can be merged when their distances are less than $2r$. As an example, the crystal structure solution of minium (Pb_3O_4) is shown in Fig. 1.1.27. In this example, special positions are identified when two oxygen or lead atoms approach within a distance less than the sum of their respective merging radii, which is estimated as 0.7 Å. The occupancies of the sites then become: 1/(1 + intersection fractional volumes).

The power of the Rietveld approach lies in its ability to extract the maximum information from the region of the data where peaks overlap. Since peak overlap is a significant problem even at moderate d-spacings, this method revolutionized powder diffraction to the point where the quantitative results are often trusted more than those coming from refinements of single-crystal data, since they are less sensitive to factors such as extinction that can affect single-crystal structure refinements. Single-crystal data are still preferred for structure solution, but Rietveld refinement is often the method of choice for obtaining the fine quantitative details of the structure after a solution has been found. However, the Rietveld method has also opened the door to using powder data for structure solution. In structure-solution methods, the structure factors are calculated from the intensities of all the available peaks, and algorithms are used to find the missing phases for each of these peaks and therefore the positions of the atoms in the unit cell. As mentioned above, full

profile fitting following the Rietveld method can be carried out without a model, where the 'parameters' are the Bragg-peak intensities themselves; this is known as Pawley or Le Bail refinement, depending on details of the approach used (see Chapter 3.5). This allows more accurate determination of the structure factors from Bragg peaks in regions where there is significant peak overlap.

These days, with high-quality data from synchrotron X-ray sources and excellent algorithms (either direct methods or global-optimization methods in direct space), determination of even quite complex crystal structures from powder diffraction data is becoming a routine method in almost all branches of natural sciences and engineering. The success rate mainly depends on three parameters: the choice of measurement device, how well the pattern profile is described and how good the structure-solving algorithm is. It is becoming increasingly evident that the use of highly monochromatic parallel-beam synchrotron radiation is a huge advantage for obtaining accuracy in the atomic parameters, which allows for the interpretation of bonding and reaction mechanisms. In some cases, even details like rotational disorder can be extracted from powder diffraction data if maximum-entropy methods are combined with high-resolution synchrotron data.

1.1.6.2. *Local structure refinement*

As described in Section 1.1.5.3.2, similar full-profile-fitting strategies are now also carried out on total-scattering data that include diffuse-scattering intensity residing in what used to be considered as the 'background'. This is either done by taking a structural model, which may be similar to the crystal model used in the Rietveld method (but the crystallographic symmetry of the model could also be reduced) or be a discrete cluster or molecule. As with the Rietveld method, structural parameters are varied in such as way as to obtain a good fit of the calculated function to the measured one. These methods go beyond the average structure and yield information about the local structure in the material, which may be different from the long-range ordered (LRO) crystal structure (or indeed there may be no LRO structure, as is the case in liquids and glasses). They are becoming more popular as data quality and computational power increase.

Solving the structures of nanoparticles from PDF data is less well developed, although it has been demonstrated for some simple structures such as C_{60} and simple inorganic crystalline compounds. We expect that this will grow in importance in the coming years, following the trend of the Rietveld method and structure solution from powders.

1.1.6.3. *Parametric Rietveld refinement*

The conventional approach to analysing a set of powder patterns is to treat each powder pattern independently, thus refining the entire set of all relevant parameters for each pattern separately. Further analysis of the values of these parameters, for example fitting with empirical or physics-based functions such as fitting the temperature dependence of the ADPs with a Debye model, is then performed after the Rietveld refinements. Alternatively, all powder patterns can be subjected to refinement simultaneously, which allows the refinement of the functional dependence of external variables instead of deriving the parameters of the function from the individual Rietveld refinements afterwards. This so-called parametric or surface Rietveld refinement was first introduced by Stinton & Evans (2007). Parametric refinement offers several advantages over the traditional sequential refinement approach because the correlation between parameters and the final standard uncertainty can be reduced by introducing simple and physically meaningful constraints and restraints. Furthermore, it is possible to refine noncrystallographic parameters such as rate constants or temperatures directly from Rietveld refinement (Stinton & Evans, 2007). Of course, introducing external constraints in this way may introduce bias into the refinement if the constraint is not valid. For example, if there is anharmonicity in the motion and the temperature dependence of the ADPs does not follow the Debye law, carrying out a parametric refinement where the Debye law is presumed will result in biased refinements. However, with careful application, this is a potentially powerful approach to maximizing the quantitative information available from powder data in complex systems. In the following, the basic concept of parametric refinement is illustrated with several examples.

If we assume a set of $p_{\max}$ powder patterns from a single sample that have been measured as a function of the value of an external variable, *e.g.* time, temperature or pressure, equation (1.1.92) can be formally written for each powder pattern separately:

$$\begin{aligned}
&Y\mathrm{calc}_{i,\mathrm{pattern}(1)} = \mathrm{function}(p_{1,\mathrm{pattern}(1)}, p_{2,\mathrm{pattern}(1)}, \ldots, p_{m,\mathrm{pattern}(1)})\\
&Y\mathrm{calc}_{i,\mathrm{pattern}(2)} = \mathrm{function}(p_{1,\mathrm{pattern}(2)}, p_{2,\mathrm{pattern}(2)}, \ldots, p_{m,\mathrm{pattern}(2)})\\
&Y\mathrm{calc}_{i,\mathrm{pattern}(p_{\max})}\\
&\quad = \mathrm{function}(p_{1,\mathrm{pattern}(p_{\max})}, p_{2,\mathrm{pattern}(p_{\max})}, \ldots, p_{m,\mathrm{pattern}(p_{\max})}).
\end{aligned} \tag{1.1.93}$$

If a functional dependency of some of the parameters p on external variables T exists, these parameters may be expressed as functions of these variables, for example T. This functional relationship can be used to constrain together the p parameters for individual patterns measured at different temperatures, drastically reducing the number of global parameters. Equation (1.1.93) can thus be written as

$$\begin{aligned}
&Y\mathrm{calc}_{i,\mathrm{pattern}(1)}\\
&= \mathrm{function}\big(p_{1,\mathrm{pattern}(1)}, p_{2,\mathrm{pattern}(1)} = f(T_1, T_2, \ldots, T_t), \ldots, p_{m,\mathrm{pattern}(1)}\big)\\
&Y\mathrm{calc}_{i,\mathrm{pattern}(2)}\\
&= \mathrm{function}\big(p_{1,\mathrm{pattern}(2)}, p_{2,\mathrm{pattern}(2)} = f(T_1, T_2, \ldots, T_t), \ldots, p_{m,\mathrm{pattern}(2)}\big)\\
&\vdots\\
&Y\mathrm{calc}_{i,\mathrm{pattern}(p_{\max})}\\
&= \mathrm{function}\big(p_{1,\mathrm{pattern}(p_{\max})}, p_{2,\mathrm{pattern}(p_{\max})} = f(T_1, T_2, \ldots, T_t),\\
&\qquad \ldots, p_{m,\mathrm{pattern}(p_{\max})}\big).
\end{aligned} \tag{1.1.94}$$

The cost function (1.1.91) to be minimized changes accordingly:

$$R_w = \sum_{\mathrm{pattern}=1}^{p_{\max}} \left(\sum_{i=0}^{n-1} \left(w_{i,\mathrm{pattern}} \big(Y\mathrm{obs}_{i,\mathrm{pattern}} - Y\mathrm{calc}_{i,\mathrm{pattern}} \big)^2 \right) \right). \tag{1.1.95}$$

1.1.7. Outlook

As is evident from the above, the information content in a powder diffraction pattern is enormous. This chapter gives only an overview of the types of information about materials that can be obtained from powder diffraction data, and the various approaches mentioned here are described in greater detail in the rest of this volume. The powder community is growing, as is the number of applications of powder diffraction in all the materials

sciences as instrumentation and computer modelling become ever more powerful. Although intense modern X-ray and electron sources can measure data from tiny single crystals (of a size approaching that of a single powder grain), this does not diminish the usefulness and impact of powder diffraction, as powder diffraction is much more than just crystal structure solution. It probes real materials in real environments, yielding information about defects, texture, nanostructure, strain, phase composition, kinetics, phase transformations, size and shape distributions, and heterogeneity. In short, crystallography gives us the structure, but powder diffraction allows us to study the 'materials science', of materials.

References

Billinge, S. J. L., Davies, P. K., Egami, T. & Catlow, C. R. A. (1991). *Deviations from planarity of copper-oxygen sheet in $Ca_{0.85}Sr_{0.15}CuO_2$. Phys. Rev. B*, **43**, 10340–10352.

Bragg, W. L. (1913). *The diffraction of short electromagnetic waves by a crystal. Proc. Camb. Philos. Soc.* **17**, 43–57.

Bruker-AXS (2007). *TOPAS* version 4.1. Bruker-AXS, Karlsruhe, Germany.

Burkel, E. (1991). *Inelastic Scattering of X-rays With Very High Energy Resolution*. Springer Tracts in Modern Physics. Amsterdam: Springer-Verlag.

Cheary, R. W. & Coelho, A. (1992). *A fundamental parameters approach to X-ray line-profile fitting. J. Appl. Cryst.* **25**, 109–121.

Compton, A. H. (1923). *A quantum theory of the scattering of X-rays by light elements. Phys. Rev. Lett.* **21**, 483.

Cooper, M. J., Mijnarends, P. E., Shiotani, N., Sakai, N. & Bansil, A. (2004). *X-ray Compton Scattering*. Oxford University Press.

Debye, P. (1912). *Zur Theorie der spezifischen Wärmen. Ann. Phys.* **344**, 789–839.

Debye, P. (1915). *Dispersion of Röntgen rays. Ann. Phys.* **46**, 809–823.

Debye, P. & Scherrer, P. (1916). *Interferenzen an regellos orientierten Teilchen im Röntgenlicht. Nachr. Ges. Wiss. Göttingen*. **29**, 1–15.

Dinnebier, R. E. & Billinge, S. J. L. (2008). Editors. *Powder Diffraction: Theory and Practice*, 1st ed. London: Royal Society of Chemistry.

Egami, T. & Billinge, S. J. L. (2013). *Underneath the Bragg Peaks: Structural Analysis of Complex Materials*, 2nd ed. Amsterdam: Elsevier.

Ewald, P. P. (1921). *Das reziproke Gitter in der Strukturtheorie. Z. Kristallogr.* **56**, 129–156.

Favre-Nicolin, V. & Černý, R. (2004). *Fox: Modular approach to crystal structure determination from powder diffraction. Mater. Sci. Forum*, **443–444**, 35–38.

Frandsen, B. A. & Billinge, S. J. L. (2015). *Magnetic structure determination from the magnetic pair distribution function (mPDF): ground state of MnO. Acta Cryst.* A**71**, 325–334.

Goodwin, A. L., Tucker, M. G., Cope, E. R., Dove, M. T. & Keen, D. A. (2005). *Model-independent extraction of dynamical information from powder diffraction data. Phys. Rev. B*, **72**, 214304.

Graf, M. J., Jeong, I. K., Starr, D. L. & Heffner, R. H. (2003). *Limits on phonon information extracted from neutron pair-density functions. Phys. Rev. B*, **68**, 064305.

Hull, A. W. (1917). *A new method of X-ray crystal analysis. Phys. Rev.* **10**, 661–696.

Jeong, I.-K., Proffen, T., Mohiuddin-Jacobs, F. & Billinge, S. J. L. (1999). *Measuring correlated atomic motion using X-ray diffraction. J. Phys. Chem. A*, **103**, 921–924.

Juhás, P., Cherba, D. M., Duxbury, P. M., Punch, W. F. & Billinge, S. J. L. (2006). *Ab initio determination of solid-state nanostructure. Nature*, **440**, 655–658.

Klug, H. P. & Alexander, L. E. (1974). *X-ray Diffraction Procedures*, 2nd ed. New York: John Wiley.

Laue, M. von (1912). *Eine quantitative Prüfung der Theorie für die Interferenz-Erscheinungen bei Röntgenstrahlen. Sitzungsber. K. Bayer. Akad. Wiss.* pp. 363–373. [Reprinted in *Ann. Phys.* (1913), **41**, 989–1002.]

Le Bail, A., Duroy, H. & Fourquet, J. L. (1988). *Ab-initio structure determination of $LiSbWO_6$ by X-ray powder diffraction. Mater. Res. Bull.* **23**, 447–452.

Levashov, V. A., Billinge, S. J. L. & Thorpe, M. F. (2005). *Density fluctuations and the pair distribution function. Phys. Rev. B*, **72**, 024111.

Masadeh, A. S., Božin, E. S., Farrow, C. L., Paglia, G., Juhás, P., Billinge, S. J. L., Karkamkar, A. & Kanatzidis, M. G. (2007). *Quantitative size-dependent structure and strain determination of CdSe nanoparticles using atomic pair distribution function analysis. Phys. Rev. B*, **76**, 115413.

Mittemeijer, E. J. & Welzel, U. (2012). Editors. *Modern Diffraction Methods*. Weinheim: Wiley-VCH Verlag GmbH.

Paddison, J. A. M. & Goodwin, A. L. (2012). *Empirical magnetic structure solution of frustrated spin systems. Phys. Rev. Lett.* **108**, 017204.

Pawley, G. S. (1981). *Unit-cell refinement from powder diffraction scans. J. Appl. Cryst.* **14**, 357–361.

Petkov, V., Billinge, S. J. L., Shastri, S. D. & Himmel, B. (2000). *Polyhedral units and network connectivity in calcium aluminosilicate glasses from high-energy X-ray diffraction. Phys. Rev. Lett.* **85**, 3436–3439.

Rietveld, H. M. (1967). *Line profiles of neutron powder-diffraction peaks for structure refinement. Acta Cryst.* **22**, 151–152.

Rietveld, H. M. (1969). *A profile refinement method for nuclear and magnetic structures. J. Appl. Cryst.* **2**, 65–71.

Shmueli, U. (2008). Editor. *International Tables for Crystallography*, Vol. B, *Reciprocal Space*, 3rd ed. Chichester: Wiley.

Squires, G. L. (1996). *Introduction to the Theory of Thermal Neutron Scattering*. New York: Dover Publications.

Stinton, G. W. & Evans, J. S. O. (2007). *Parametric Rietveld refinement. J. Appl. Cryst.* **40**, 87–95.

Warren, B. E. (1990). *X-ray Diffraction*. New York: Dover Publications.